Structural basis for coupling of the WASH subunit FAM21 with the endosomal SNX27-Retromer complex

Qian Guo[1,†], Kai-en Chen[1,†], Manuel Gimenez-Andres[2,†], Adam P. Jellett[2], Ya Gao[1], Boris Simonetti[2], Meihan Liu[1], Chris M. Danson[2], Kate J. Heesom[3], Peter J. Cullen[2,‡], Brett M. Collins[1,‡].

[1] The University of Queensland, Institute for Molecular Bioscience, St Lucia, Queensland, 4072, Australia.

[2] School of Biochemistry, Faculty of Life Sciences, Biomedical Sciences Building, University of Bristol, Bristol BS8 1TD, UK.

[3] Bristol Proteomics Facility, School of Biochemistry, Faculty of Life Sciences, Biomedical Sciences Building, University of Bristol, Bristol BS8 1TD, UK.

[†]Contributed equally

[‡]Corresponding author: pete.cullen@bristol.ac.uk; b.collins@imb.uq.edu.au

Running title: SNX27-Retromer interaction with WASH.

ABSTRACT

Endosomal membrane trafficking is mediated by specific protein coats and formation of actin-rich membrane domains. The Retromer complex coordinates with sorting nexin (SNX) cargo adaptors including SNX27, and the SNX27–Retromer assembly interacts with the WASH complex which nucleates actin filaments establishing the endosomal reycling domain. Crystal structures, modelling, biochemical and cellular validation reveal how the FAM21 subunit of WASH interacts with both Retromer and SNX27. FAM21 binds the FERM domain of SNX27 using acidic-Asp-Leu-Phe (aDLF) motifs similar to those found in the SNX1 and SNX2 subunits of the ESCPE-1 complex. Overlapping FAM21 repeats and a specific Pro-Leu containing motif bind three distinct sites on Retromer involving both the VPS35 and VPS29 subunits. However, mutation of the major VPS35-binding site does not inhibit cargo recycling, indicating that a network of redundant interactions promote endosomal activity of the WASH complex. These studies establish the molecular basis for how SNX27–Retromer is coupled to the WASH complex via overlapping and multiplexed motif-based interactions required for the dynamic assembly of endosomal membrane recycling domains.

INTRODUCTION

Maintenance of appropriate levels of endosomal sorting of transmembrane 'cargo' proteins is essential for cellular function (Cullen & Steinberg, 2018). Mammalian Retromer is an evolutionarily conserved protein complex composed of VPS35, VPS29, and VPS26 (two isoforms VPS26A and VPS26B) and is a central regulator of endosomal sorting across eukaryotes (Burd & Cullen, 2014; Chen *et al*, 2019). More specifically, it functions together with diverse accessory proteins and cargo adaptors to coordinate endosomal recruitment and sequence-specific cargo recognition with the assembly of endosomal sub-domains for the biogenesis of tubulovesicular transport carriers. Sorting nexin 27 (SNX27) is a Retromer cargo adaptor that binds to specific PSD95-DLG-ZO1 (PDZ) domain binding motif (PDZbm) containing cargo to promote their Retromer-dependent endosome-to-cell surface recycling (Lunn et al., 2007; Lauffer et al., 2010; Temkin et al., 2011; Steinberg et al., 2103; Gallon et al., 2014; Clairfeuille et al., 2016).

Both Retromer and SNX27 associate with the Wiskott-Aldrich Syndrome Protein and SCAR Homolog (WASH) complex, which by driving localised actin polymerisation plays an essential role in endosomal sorting and transport (Derivery *et al*, 2009; Gomez & Billadeau, 2009; Gomez *et al*, 2012; Harbour *et al*, 2010; Harbour *et al*, 2012; Steinberg *et al*, 2013; Temkin *et al*, 2011). The WASH complex is a pentamer of WASHC1, FAM21 (WASHC2), WASHC3 (coiled-coil domain-containing protein 53 (CCDC53)), WASHC4 (KIAA1033; WASH-interacting protein; SWIP) and WASHC5 (Strumpellin; KIAA0196) (Derivery *et al.*, 2009; Gomez & Billadeau, 2009; Jia *et al*, 2010; Valdmanis *et al*, 2007). The WASHC1 subunit is a member of the Wiskott-Aldrich Syndrome Protein (WASP) family (Jia *et al.*, 2010; Padrick & Rosen, 2010), and the presence of a C-terminal verprolin homology sequence, connecting sequence, and acidic sequence (VCA) domain allows WASHC1 to activate the actin-related protein 2/3 (ARP2/3) complex to stimulate formation of branched F-actin networks (Burianek & Soderling, 2013). The ARP2/3 complex plays a number of roles in regulating endocytosis and subsequent endosomal sorting and transport processes (Chakrabarti *et al*, 2021; Duleh & Welch, 2010; Park *et al*, 2013).

During endosomal cargo sorting and transport, the WASH complex is essential for the fission of tubules during the biogenesis of transport carriers. Endosomal tubulation is exaggerated in cells lacking the WASH complex (Gomez & Billadeau, 2009) and WASH depletion leads to the observation of long endosomal tubules aligned along microtubules (Derivery *et al.*, 2009). It is thought that WASH promotes the scission of cargo-containing tubules via generating F-actin-driven force at the endosomal membrane. Mutations in WASH complex subunits can result in neurological pathologies, such as hereditary spastic paraplegia, inherited intellectual disability, and late-onset Alzheimer's disease (de Bot *et al*, 2013; Ropers *et al*, 2011; Valdmanis *et al.*, 2007; Vardarajan *et al*, 2012).

Retromer regulates the recruitment of a population of the WASH complex to endosomal membranes (Harbour *et al.*, 2010; Harbour *et al.*, 2012), while binding of WASHC4 to membrane phosphoinositide lipids can promote Retromer-independent mechanism of endosomal association (Dostal et al., 2023). Native immunoprecipitations provided the initital evidence for the WASH complex interacting with Retromer, while yeast two-hybrid assays suggested direct associations between VPS35, FAM21 and WASHC1 (Harbour *et al.*, 2010). Suppression and knock-out of Retromer partly reduces WASH endosomal association

(Harbour et al., 2010; McNally et al., 2017), while other members of the endosomal protein sorting system are unaffected, such as SNX1 and the RAB5 effector EEA1 (Harbour *et al.*, 2010). Structurally, FAM21 has a 200 amino acid "head" domain that interacts with the Strumpellin and WASHC1 proteins and is crucial for the formation and stabilisation of the WASH complex (Harbour *et al.*, 2012; Jia *et al.*, 2010). Following the head domain is a large (around 1100 amino acids) unstructured "tail" domain that contains 21 repeating motifs composed of Leu-Phe and several acidic residues (Asp or Glu) dubbed LFa motifs (Jia *et al*, 2012). The enormous unstructured tail of FAM21 is important for membrane association (Gomez & Billadeau, 2009), and it was shown that the LFa motifs can bind to the VPS35 subunit of Retromer with the C-terminal motifs most crucial for the interaction (Helfer *et al*, 2013; Jia *et al.*, 2012). Overexpression of the FAM21 tail can displace the WASH complex on the endosome by competing for binding to VPS35 (Harbour *et al.*, 2012; Helfer *et al.*, 2013; Jia *et al.*, 2012). Although the VPS35 subunit can associate with the FAM21 tail directly in yeast two-hybrid experiments and in isothermal titration calorimetry (ITC) assays (Harbour *et al.*, 2012; Jia *et al.*, 2012), binding is enhanced by other subunits when VPS35 is assembled into the functionally active Retromer complex (Helfer *et al.*, 2013). The interaction of Retromer with WASH via FAM21 is thought to link branched actin polymerisation to cargo protein sorting and trafficking activity, and the long unstructured nature of the FAM21 tail combined with the many LFa repeats likely promotes both avidity for Retromer and flexibility in the relative orientations for dynamic endosomal membrane sorting.

The SNX27 Retromer cargo adaptor was also reported to associate with the WASH complex by coimmunoprecipitation (Steinberg *et al.*, 2013). Responsible for recycling over 400 specific transmembrane cargoes from endosomes to the plasma membrane (Balana *et al*, 2011; Gallon *et al*, 2014; Ghai *et al*, 2011; Ghai *et al*, 2015; Steinberg *et al.*, 2013), SNX27 is a peripheral membrane protein containing, from N-termini to C-termini, PDZ, PX and FERM domains that mediate cargo selection, Retromer recruitment and protein-lipid interactions (Clairfeuille *et al*, 2016; Ghai *et al.*, 2015; Li *et al*, 2019). Notably, SNX27 can bind via its FERM domain to acidic DLF (aDLF) motifs in the N-terminal disordered region of SNX1 and its homologue SNX2 within the BAR domain-containing ESCPE-1 complex (Simonetti *et al*, 2022; Yong *et al*, 2021).

Here we show that the FAM21 subunit of WASH coordinates the interactions with both Retromer and SNX27 via very different mechanisms but incorporating distinct overlapping elements of the repeat sequences in its extended C-terminal domain. Crystal structures, modelling, biochemical and cellular experiments show that the multiple redundant acidic-Asp-Leu-Phe (aDLF) repeat sequences in FAM21 bind to a conserved basic pocket in the SNX27 FERM domains and are essentially identical to the aDLF sequences found in the endosomal proteins SNX1 and SNX2 (Simonetti *et al.*, 2022). Overlapping repeated motifs in FAM21 with the consensus sequence [L/I]F[ED]$_{3\text{-}9}$[L/I]F bind two conserved sites towards the C-terminus of Retromer subunit VPS35. These lie opposite to the VSP29 binding site and adjacent to the dimerising surface required for assembling Retromer arches on the membrane. In addition, the last repeat of FAM21 contains a specific Asp-Pro-Leu sequence that binds a third site on VPS29 that is the same region bound by other interactors such as TBC1D5 and ANKRD27. Mutations in these regions perturb FAM21 interaction *in vitro* and in cells, however single mutations in VPS35 are not sufficient to block Retromer-

mediated trafficking, consistent with a model whereby the WASH complex engages the endosome and associated proteins through multiple related but redundant motif-mediated interactions.

RESULTS

The FAM21 tail binds to both VPS35 and VPS29 through its repeat sequences

A primary characteristic of FAM21 is the long disordered tail enriched in acidic residues and containing 21 copies of a repeated [I/L]F sequence with C-terminal acidic residues (**Figures 1A and 1B**). This was previously termed the LFa motif and shown to bind directly to the Retromer subunit VPS35 with the final three repeats, 19-21, showing the strongest binding affinity (Jia *et al.*, 2012). However, suggesting that VPS29 also plays a role in binding FAM21, we recently noted that binding of Retromer and GST-tagged FAM21 composed of repeats 19, 20 and 21 (GST-FAM21$_{R19-R21}$) was slightly reduced in the presence of a macrocyclic peptide that binds via a PL-containing sequence to a conserved site on the VPS29 subunit (Chen *et al*, 2021). To examine this, we first tested the binding between Retromer and peptides from human FAM21 repeat 19 (FAM21$_{R19}$), repeat 20 (FAM21$_{R20}$) and repeat 21 (FAM21$_{R21}$). Using ITC, we found FAM21$_{R21}$ alone was able to bind to Retromer, to the subcomplex composed of VPS29 and VPS35 residues 481 to 796 (VPS29–VPS35$_{481-796}$), as well as VPS29 alone (**Figure 1C; Table S1**). In contrast, FAM21$_{R19}$ and FAM21$_{R20}$ peptides showed a relatively weak Retromer interaction and no interaction at all with VPS29 (**Figure 1C)**. A stronger Retromer interaction was observed when we tested the GST-tagged construct combining repeats 19 and 20 (GST-FAM21$_{R19-R20}$), suggesting some additive effect of these two sequences (**Figure 1D)**. Notably the FAM21$_{R21}$ interaction with VPS29 on its own could be blocked by the addition of cyclic peptide RT-D1 (**Figure 1E**), indicating that FAM21$_{R21}$ likely binds to the same conserved VPS29 surface. Unlike other repeats FAM21 repeat 21 also contains a conserved DPL sequence next to the [I/L]Fa motif (**Figure 1B; Figure S1**) and it is this sequence that binds to VPS29 while other repeats bind to VPS35.

Structural basis for the interaction of FAM21 LFa repeats with VPS35

Our data suggests that FAM21 LFa repeats 19 and 20 interact with VPS35 while the divergent DPL-containing repeat 21 can bind VPS29. To understand the molecular basis of how the LFa repeating units bind to Retromer, we attempted to co-crystallize the VPS29–VPS35$_{481-796}$ subcomplex with FAM21$_{R19}$ and FAM21$_{R20}$ peptides. The structure of VPS29–VPS35$_{481-796}$ in complex with FAM21$_{R20}$ peptide was successfully solved at 3 Å resolution with two VPS29–VPS35$_{481-796}$ molecules in the asymmetric unit (**Figure 2A; Table S2**). Although the structure was solved at relatively low resolution, we could observe additional electron density on the surface of VPS35 representing the FAM21$_{R20}$ peptide (**Figure 2B**). The electron density for the FAM21$_{R20}$ peptide is located on a conserved positively charged groove of VPS35 between helices 23 and 25 surrounded by K552, K555, K556 and K559 (**Figures 2B and 2C**). To aid in assigning the FAM21$_{R20}$ residues into the structure as well as investigate the potential binding surface of repeat 19, we used AlphaFold2 modelling to predict complexes of different variations of FAM21 sequences bound to Retromer. These predictions consistently identified two separate binding sites on VPS35 for the FAM21$_{R19-R20}$ LFa repeats (**Figures 2D and 2E**). Inspecting these models closely, we found that repeats 19 and 20 are predicted to bind two distinct positively charged grooves at the C-terminal end of the VPS35 surface that we refer to as Site 1 and Site 2 respectively (**Figure 2E**). The X-ray crystallographic difference density for FAM21$_{R20}$ peptide aligns with Site 2 and matches well to the residues ^{1296}DDIF^{1299} of repeat 20

predicted in the model (**Figure 2F**). In particular I1298 and F1299 are positioned to interact with K555, K556 and K559 of VPS35 (**Figure 2F**). A notable feature of the predicted structure is that in addtion to the ^{1296}DDIF^{1299} residues the repeated element engages VPS35 via an additional IF sequence interspersed with acidic residues ^{1290}IFDDDMDDIF^{1299} (**Figure 2F**). Similarly the predictions indicate that the second R19 sequence can bind to Site 1 with a similar dual [I/L]F motif with interspersed acidic residues ^{1262}LFDDNIDIF^{1270} recognising a second positively charged groove composed of K701, K705 and K749 (**Figure 2E**). With the combination of predictions and experimental structure we propose that VPS35 possesses two distinct binding sites for low affinity binding of the multiple LFa sequences in FAM21 (**Figure 1B**)(Jia *et al.*, 2012). These structures indicate the definition of the LFa motif to ideally possess two [I/L]F sequences with an interveining stretch of Asp and Glu side chains [I/L]F[E/D]$_n$[I/L]F.

To further validate if both positively charged grooves of VPS35 are responsible for binding to FAM21 we performed co-immunoprecipitation with structurally targeted site-directed mutations of VPS35. Importantly, all mutants retained the ability to assemble into the Retromer heterotrimeric complex **(Figure 2G and 2H; Figure S2)**. Consistent with our structural data, binding to FAM21 was significantly affected by the multiple mutations around the repeat 20 binding grooves including K552, K555, K556 and K559 (**Figure 2G; Figure S2**). The strongest defect in FAM21 binding was observed with the triple mutant composed of K555, K556 and K559 (**Figures 2G and 2I; Figure 2G; Figure S2**), the residues known to form contact with the LFa motif in Site 2. In addition, mutations of other positively charged residues surrounding the core [I/L]F dipeptide including K515S also showed significant defects in binding. It is likely that these residues together form a large positively charged patch on VPS35 for the initial recognition of the acidic repeats of FAM21. A similar defect was also observed in the K701E mutant on the second positively charged groove of Site 1 (**Figure 2H**). Notably, we also observed a slight defect in FAM21 binding when we used the VPS35 D620N mutant, the mutation known to be involved in the Parkinson diseases (McGough et al., 2014; Zavodszky et al., 2014). The mutation is distal from the FAM21$_{R19}$ and FAM21$_{R20}$ binding sites but lies next to the VPS35-mediated Retromer dimerization interface as seen in the Retromer-SNX3 and Retromer-SNX-BAR tubular coat complexes (Leneva *et al*, 2021) (**Figure 2J**). It is possible that the slight defect in FAM21 binding is indirectly caused by interference with Retromer dimerization.

Repeat 21 binds to VPS29 through a classic PL motif interaction

To better understand the association of FAM21 repeat 21 with Retromer we next crystallised the VPS29–VPS35$_{481-796}$ complex with the FAM21$_{R21}$ repeat and determined its crystal structure at a modest 3.4 Å resolution. The structure reveals two VPS29–VPS35$_{481-796}$ molecules in the asymmetric unit. Notably, the dimerization interface in this structure differ from that observed in the FAM21$_{R20}$ bound structure (**Figure 3A**). Depsite the low resolution, we could still observe additional electron density around the conserved hydrophobic pocket of VPS29 (**Figure 3A**). To unambiguously assign the key residues involve in the interaction, we then successfully solved the structure of the VPS29–FAM21$_{R21}$ peptide complex at 2.0 Å resolution (**Figure 3B**). The improved density allowed us to build the PL motif and upstream residues. According to the structure, we could unambiguously observe the density up to D1332, suggesting that the

signature [I/L]Fa dipeptide located at position 1330 and 1331 was not involved in the binding (**Figure 3C**). In direct contrast to the $FAM21_{R20}$ structure bound with VPS35, the $FAM21_{R21}$ reveals a typical PL motif binding mode to VPS29 that superposes well with the previous cyclic peptide structures (**Figure 3D**) and other previous complexes with RidL, TBC1D5, VARP and VPS35L (Boesch *et al*, 2023; Healy *et al*, 2023; Jia *et al*, 2016; Laulumaa *et al*, 2023; Romano-Moreno *et al*, 2017).

Consistent with the two structures and our mutagenesis studies, AlphaFold2 predictions incorporating the FAM21 sequence with all three repeats 19-21 produce a model with the three repeats bound to the three distinct sites; R19 and R20 respectively binding Site 1 and Site 2 on VPS35 and R21 extending around to bind to the conserved VPS29 surface (**Figure 3E-3H**). Both $FAM21_{R20}$ and $FAM21_{R21}$ peptide observed in the crystal structures fit well to the various models generated by Alphafold2 (**Figure 3G**). It seems very likely other LFa repeats would have the capacity to interact with one or both sites in VPS35. Indeed further analysis using Alphafold2 supports the potential of other repeats to bind VPS35 with similar structures (**Figures 3H; Figure S3**), and we find that repeats 5 and 17 (although not repeat 15), show low affinity for Retromer (**Figure 3I**). Projecting these findings onto the VPS35-mediated Retromer dimer observed in cryotomography structures (Leneva *et al.*, 2021), we expect that the LFa repeats such as $FAM21_{R19,}$ $FAM21_{R20}$ and $FAM21_{R21}$ can potentially use at least two distinct binding modes to engage the membrane-associated Retromer complex. With Repeat 21 bound to VPS29 as the reference point, repeats 19 and 20 and other LFa repeats from FAM21 could physically associate with two adjacent Retromer complexes in *trans* (model 1) or with one copy of Retromer in *cis* (model 2) (**Figure 3J**).

Interaction of FAM21 aDLF motifs with the SNX27 FERM domain

In addition to Retromer, SNX27 has also been reported to bind FAM21 to enable proper cargo recycling (Kvainickas *et al*, 2017; Lee *et al*, 2016; Steinberg *et al.*, 2013). To confirm this interaction, we first examined the binding using co-immunoprecipitations with various truncation constructs of GFP-FAM21. Robust association was observed between SNX27 and C-terminal region of FAM21(1109-1341) and FAM21(1250-1341) (**Figure 4A**). A shorter construct of FAM21(1300-1341) however, which lacks all LFa repeats apart from repeat 21, was unable to bind. Using ITC, we found that full-length human SNX27 bound to GST-tagged $FAM21_{R19\text{-}21}$ with a K_d of ~6 μM (**Figure 4B; Table S3**). Similar binding affinity was also detected when the FERM domain ($SNX27_{FERM}$) was used instead of the full-length SNX27 (**Figure 4B**), suggesting that the interaction primarily occurs through the FERM domain. We also tested the binding of $SNX27_{FL}$ and $SNX27_{FERM}$ with peptides corresponding to individual repeats $FAM21_{R19}$, $FAM21_{R20}$ and $FAM21_{R21}$ (**Figure 4C and D**). The results further reinforced the co-immunoprecipitation experiments showing that both $FAM21_{R19}$ and $FAM21_{R20}$ peptides bind to SNX27 with a K_d of ~7 μM and ~20 μM respectively, while repeat 21 showed no detectable interaction.

We noted that LFa repeats 19 and 20 (but not repeat 21) also contain sequences that resemble the acidic DLF (aDLF) motifs found in SNX1 and SNX2 previously shown to bind to the FERM domain of SNX27 (Simonetti *et al.*, 2022). Indeed, mutations in the $FAM21_{R20}$ peptide substituting the DIF sequence with DSS blocked interaction with $SXN27_{FL}$ completely (**Figure 4E**), indicating that the D[L/I]F motif

within repeats 19 and 20 play a major role in binding to SNX27. Sequence analysis of all of the 21 repeats within FAM21, showed that 12 of them also included the same sequence pattern with poly-acidic resides in front of a conserved D[L/I]F motif (**Figure 4F**). We proposed that all of these repeats are potentially able to bind SNX27, and using $FAM21_{R5}$, $FAM21_{R8}$, $FAM21_{R15}$ and $FAM21_{R17}$ peptides as examples we found all four showed micromolar binding affinity to $hSXN27_{FERM}$ (**Figures 4G and 4H**). These ITC data together confirmed that the D[L/I]F motif is the main region responsible for binding to the FERM domain of SNX27, while the poly-acidic residues prior to the D[L/I]F motif play a critical role in facilitating the association.

FAM21 and SNX1/SNX2 share the same binding pocket in the SNX27 FERM domain.

To confirm the molecular basis for how FAM21 binds to SNX27, we first applied Alphafold2 to predict models of $SNX27_{FERM}$ in complex with the subset of FAM21 repeats containing the putative aDLF motifs. Consistent with our expectation, all the FAM21 repeats were predicted to bind the same conserved pocket on the F3 module of the SNX27 FERM domain (**Figure S4**), also known to bind to the aDLF motifs from SNX1/SNX2 (Simonetti *et al.*, 2022; Yong *et al.*, 2021). To validate the models we then co-crystallized $SNX27_{FERM}$ with several different FAM21 repeat motifs and crystal structures were determined with $FAM21_{R15}$, $FAM21_{R19}$ and $FAM21_{R20}$. All three complexes were solved in the same space group showing a single FERM domain in the asymmetric unit (**Figures 5A-5C; Table S4**). The electron density of the aDLF motif region was clearly visible in the highly conserved positively charged pocket of the SNX27 FERM domain (**Figures 5A-5C**). Superimposition of the three structures revealed a high degree of similarity without any major differences (**Figures 5D and 5E**). Our structures also superposed well to the SNX1 peptide bound complex published previously (Simonetti *et al.*, 2022; Yong *et al.*, 2021) (**Figure 5F**).

To confirm the binding mode of SNX27 binding to FAM21 aDLF sequences we tested mutations in key SNX27 residues. SNX27 R437D and R498D mutants failed to interact with $FAM21_{R19}$ peptide by ITC, while K495D, K496D and K501D reduced binding compared to the wild-type SNX27 (**Figure 5G**). The same pattern of binding was observed by co-immunoprecipitation of proteins from HEK293T cells (**Figure 5H**), although interestingly the K495D, K496D and K501D mutants had a greater impact on the ESCPE-1 complex interaction (represented by SNX6 in these experiments) than FAM21 and the WASH complex. This suggests that R437D and R498D play a central role in forming contacts with both FAM21 and SNX1/SNX2-derived aDLF peptides. In particular, R498 is likely to be responsible for electrostatic attraction with the poly-acidic residues in front of the aDLF motifs. Indeed, comparative unbiased proteomic analysis comparing the interactomes of wild-type SNX27 with the R498D mutant of SNX27 confirmed a significant reduction in association of SNX27(R498D) with subunits of both the WASH and ESCPE-1 complexes (**Figure 5I; Figure S5A; Table S2**).

Perturbing WASH association with Retromer Site 2 does not alter steady-state endosome-to-plasma membrane recycling of SNX27 cargo proteins.

We and others previously established that mutations in SNX27 that block interactions with aDLF motifs perturb endosomal retrieval and recycling of the SNX27-interacting cargo GLUT1 by the SNX27-Retromer-

ESCPE-1 pathway (Simonetti *et al.*, 2022; Yong *et al.*, 2021). While part of this complex phenotype can be ascribed through a defect in SNX1 and SNX2-containing ESCPE-1 complex binding to SNX27 during the hand-over of retrieved cargo into newly forming tubular transport carriers (Simonetti et al., 2022), our data presented here indicates that the SNX27(R498D) mutant not only perturbs SNX1/SNX2 association but also binding to the WASH complex. Thus the precise role of the SNX27 R498 pocket in the GLUT1 trafficking phenotype could be attributed to either or both of these interactions and it is not possible to design highly specific SNX27 mutations to distinquish them. In addition, the highly redundant nature of the multiple overlapping LFa/aDLF repeats in FAM21 preclude the design of single point mutations in the FAM21 tail to test the role of specific sequences. Indeed, we found that although deletion of repeats 19-21 (residues 1250-1341) in the tail could reduce both Retromer and SNX27 interactions (**Figure 4A**), individual point mutations in these repeats had no impact on binding (**Figure S5B**) demonstrating that no single sequence is required to mediate their binding.

We also assessed whether the interaction of Retromer with the WASH complex was specifically required for receptor recycling, by performing rescue experiments with the primary Site 2 VPS35 FAM21-binding mutant K555N/K556L/K559Q (see **Figure 2G and 2H**). Rescue experiments were performed in both VPS35 knock-out HeLa cells (**Figure 6**) and H4 cells (**Figure S5C**) with similar results. As expected, in VPS35 KO cells the cell surface levels of SNX27-Retromer cargos including GLUT1, and Kidins220, were reduced. When GFP-VPS35 was re-expressed the cell surface levels of these proteins recovered to normal levels. However, unexpectedly, the GFP-VPS35 (K555N/K556L/K559Q) mutant was equally able to rescue endosomal recycling of these cargos. These data show that reduced FAM21 binding to Retromer Site 2 does not reveal a quantifiable perturbation in the steady-state recycling of SNX27-Retromer-dependent cargos, although previous studies directly targeting FAM21 have shown that FAM21 depletion or knock-out does lead to cargo sorting defects (Lee *et al.*, 2016; McGough *et al*, 2014a). It is likely that these data can be reconciled through the complex multivalent nature of FAM21 association with Retromer, such that although the VPS35 Site 2 mutation reduces WASH interaction significantly (**Figure 2G and 2H**), the two other minor sites in VPS35 and VPS29 retain an ability to engage FAM21 and may compensate for its loss. Further, Fam21 can interact with SNX27 and potentially other endosomal proteins such as the Commander complex (McNally *et al*, 2017; Singla *et al*, 2019), and a population of WASH complex is associated to endosomes even in the absence of Retromer providing an added level of potential compensation (Dostal et al., 2023).

DISCUSSION

In this work we have defined the molecular mechanisms underpinning the direct interactions between Retromer, SNX27 and the WASH complex via the extended C-terminal domain of the FAM21 subunit. These interactions firmly establish the role of highly repetitive sequences in FAM21 for directly engaging both SNX27 and Retromer using distinct but overlapping sequence requirements. LFa repeats consist of two [L/I]F motifs interspersed by tracts of acidic side chains and mediate specific Retromer attachment through VPS35. aDLF repeats consist of a D[L/I]F motif preceded by acidic residues, overlap with the LFa repeats and specifically interact with the FERM domain of SNX27 using a completely different mechanism. Combined with previous work (Harbour *et al.*, 2012; Jia *et al.*, 2012; Simonetti *et al.*, 2022), these studies lead to an evolving model for the assembly of the SNX27-Retromer-WASH endosomal recycling domain as one of extreme structural plasticity, sequence redundancy within FAM21, and molecular avidity between FAM21 and assembled oligomers of SNX27–Retromer on the endosomal membrane (**Figure 7**). This network of interactions will also incorporate other proteins known to interact with the FAM21 C-terminus, including the Commander assembly (Bartuzi *et al*, 2016; McNally *et al.*, 2017; Phillips-Krawczak *et al*, 2015; Singla *et al.*, 2019), WDR91 (Liu *et al*, 2022), RME-8 (Freeman *et al*, 2014), FKBP15 (Harbour *et al.*, 2012), as well as TBC1D23 which has also been shown to bind to FAM21's LFa repeats (Huang *et al*, 2019; Shin *et al*, 2017).

Our data shows that the LFa repeat sequences in FAM21 interact with Retromer at two distinct sites. Opposite to the VPS29-binding surface the VPS35 subunit has two separate sites for binding the peptide motifs, centred on K552, K555, K556 and K559 near the centre of the VPS35 α-helical solenoid (Site 2) and around K701, K705 and K749 near the C-terminus (Site 1). The discovery of two distinct binding pockets was surprising, and points to the potential of both redundancy in motif interactions (each site appears to have similar potential for binding FAM21 repeats) and avidity for increased binding strength (covalently connected sequences in FAM21 binding to two sites simultaneously). The presence of two binding sites is somewhat reminiscent of the binding of bipartite nuclear localisation signals to major and minor surfaces of the α-helical solenoid of importins, although the mechanisms are completely different (Christie *et al*, 2016). Although we do not observe dramatic differences between the affinities of individual and multiple FAM21 repeats for Retromer by ITC, we propose that the combination of Retromer oligomerisation on the membrane (Kovtun *et al*, 2018; Leneva *et al.*, 2021) with the multivalent nature of FAM21 interactions will promote a high level of specificity in WASH/Retromer engagement (Teilum *et al*, 2021). Given the enormous extended structure of the FAM21 tail and the number of similar LFa motifs, FAM21 will readily interact with multiple Retromer complexes when organised into polymeric arches at the endosomal membrane. It is also worth noting that this will not lead to a specific stoichiometry for the Retromer/WASH interaction, but rather will promote formation of a heterogeneous and dynamic multivalent network.

In addition to the LFa sequences binding to VPS35, we identified a third binding site on the conserved surface of VPS29 for the final repeat of FAM21 which possesses a DPL sequence. This binds with modest affinity, and is likely inessential for direct Retromer-dependent endosomal recruitment of FAM21 (**Figure S5B**) (Harbour et al., 2010; Harbour et al., 2012). We speculate however, that once the WASH

complex has bound to Retromer and/or SNX27 that repeat 21 may then act to regulate the association of Retromer with other proteins that bind the same site such as TBC1D5 (Jia *et al.*, 2016; Seaman *et al*, 2009; Seaman *et al*, 2018) or ANKRD27 (Crawley-Snowdon *et al*, 2020) (**Figure 7**).

Retromer, SNX27 and WASH are intimately connected in the endosomal sorting and transport of numerous transmembrane proteins (Fokin & Gautreau, 2021; Seaman *et al*, 2013; Simonetti & Cullen, 2019). The current model is that Retromer, along with SNX cargo adaptors such as SNX3 and SNX27, can establish endosomal retrieval sub-domains and membrane tubules enriched in cargo, and WASH is able to nucleate formation of branched actin filaments via Arp2/3 that enhance membrane tubulation and promote scission (Puthenveedu et al., 2010; Temkin et al., 2011). The capping-interacting motif (CPI) of FAM21 is responsible for recruiting uncapping dynactin mini-filaments, that then prime the WASH-induced actin branching (Fokin *et al*, 2021). The first indications that Retromer and WASH cooperate in endosomal recycling demonstrated their colocalization and a direct interaction between the FAM21 C-terminal tail and the Retromer complex (Gomez & Billadeau, 2009; Harbour *et al.*, 2010; Harbour *et al.*, 2012; Jia *et al.*, 2012). These studies also identified the 21 LFa repeats in the FAM21 tail and their importance for Retromer association (Jia *et al.*, 2012). The C-terminal tail of FAM21 is sufficient for endosomal localisation (Harbour *et al.*, 2012), and Retromer is important for endosomal recruitment of WASH (Harbour *et al.*, 2010; Helfer *et al.*, 2013; Jia *et al.*, 2012; McGough *et al*, 2014b; Zavodszky *et al*, 2014), although WASH can also be recruited through Retromer-independent mechanisms via FAM21 and WASHC4/SWIP subunits respectively (Dostál *et al*, 2022). WASH depletion was also reported to result in exaggerated endosome-derived tubules (Derivery *et al.*, 2009; Gomez & Billadeau, 2009; Ryder *et al*, 2013), although this is not universally observed (Buckley *et al*, 2016; Lee *et al.*, 2016; McGough *et al.*, 2014a; Miller *et al*, 2018).

Previous research established that the FERM domain of SNX27 associates with the aDLF motifs of SNX1 and SNX2 (Simonetti *et al.*, 2022; Yong *et al.*, 2021), and our data now shows that FAM21 utilises an identical mechanism to engage with the SNX27 adaptor. As shown in **Figure 3F**, the sequence alignment with SNX1/SNX2 peptides shows the D[L/I]F triplet is the most important component for binding, and at least two acidic amino acids before this motif are also important for promoting electrostatic interactions with SNX27. SNX1 and SNX2 are SNX-BAR proteins and subunits of the ESCPE-1 complex along with SNX5 and SNX6 (Simonetti *et al.*, 2022). Mutations targeting the aDLF motif in SNX1 or SNX2 that disrupted binding to SNX27 have highlighted the role of the SNX27-ESCPE-1 interaction in promoting the tubular-based endosomal exit and cell surface recycling of SNX27-Retromer cargo (Yong *et al*, 2021; Simonetti et al., 2022). The results here both extend these previous analyses and complicate their interpretation, as the SNX27(R498D) mutant disrupts not only ESCPE-1 binding but also FAM21 and WASH association. As it is impossible to design SNX27 mutations that only affect SNX1/SNX2 but not FAM21 binding (and *vice versa*), we currently cannot disentangle the individual roles of each interaction on SNX27-dependent trafficking, and effects could be due to either interaction or a combination of both. Overall, however, this further establishes that not only Retromer but also SNX27 serve as direct ligands for overlapping multivalent repeat sequences in the FAM21 tail.

Combined with previous studies, our work makes it clear that the formation of endosomal retrieval sub-domains involves a dynamic network of generally low affinity interactions between Retromer, SNX27, ESCPE-1 and the WASH complex (and not discussed here ANKRD50) (McGough et al., 2014; Kvainickas et al., 2017), that includes a series of polyvalent extended sequences in subunits of the ESCPE-1 and WASH complexes. Low affinity interactions ensure that coincidence sensing of cargo and accessory proteins is required to provide the avidity necessary for pathway progression. This builds into the network dynamic instability where if the correct density of cargo and accessory proteins are not sufficient, one could consider these to be 'checks and balances', then sub-domain organisation and coat formation will not be stabilised and the pathway will not progress (Schmid & McMahon, 2007). A more detailed understanding of both the spatial and temporal regulation of the interactions within the SNX27-Retromer-WASH-ESCPE-1 pathway will be challenging due to the high degree of multivalent and low affinity interactions involved, but will be essential for a complete portrait of this endosomal retrieval and recycling pathway(s). Reconstituting this pathway *in vitro* on artificial membranes, as well as high-resolution live-cell imaging will be required to begin to answer these questions, but the work here provides a key mechanistic foundation for these studies.

MATERIAL AND METHODS:

Peptides

All synthetic peptides applied for ITC and X-ray crystallography were obtained from Genscript (USA and Singapore). The peptides were freshly lyophilized using a laboratory freeze dryer Martin Christ ALPHA 1-2 LDplus to avoid chemical residues. To obtain the peptide stock solutions with a final concentration of 30 mM and a neutral pH, the freeze-dried peptides were dissolved in 1M HEPES pH 7.5. For use in ITC and co-crystallisation screening experiments, the peptides were diluted in protein buffer: 20 mM Tris-HCl pH 7.5, 200 mM NaCl, 5% glycerol, 1 mM β-ME. The sequences of peptides utilised were: FAM21-R5$_{536-552}$ GLFSDEEDSEDLFSSQS, FAM21-R8$_{662-678}$ TSLFEEDEEDDLFAIAK, FAM21-R15$_{1124-1140}$ RGEADLFDSGDIFSTGT, FAM21-R17$_{1197-1213}$ NPFPLLEDEDDLFTDQK, FAM21-R19$_{1261-1274}$ NLFDDNIDIFADLT, FAM21-R20$_{1289-1302}$ SIFDDDMDDIFSSG, FAM21-R20$_{1289-1302(IF/SS)}$ SSSDDDMDDSSSSG, and FAM21-R21$_{1328-1341}$ SNIFDDPLNAFGGQ, and they were generated from human WASH complex subunit 2A (FAM21A), Q641Q2.

Molecular biology and cloning for recombinant protein production

For bacteria expression of human Retromer and Retromer subcomplex, DNA encoding full-length Vps26A, Vps29, Vps35 and Vps35$_{481-796}$ were cloned into either pET28a or pGEX4T2 vectors as described previously (Chen *et al.*, 2021). For SNX27, the codon-optimized gene containing full-length human SNX27 was synthesized by GenScript® and cloned into pET28a vector as described previously (Simonetti *et al.*, 2022). The FERM domain containing residues 271 to 528 was inserted into pMCSG7 vector containing a N-terminal His-TEV tag. Human FAM21 truncation constructs including FAM21$_{R19-21}$, FAM21$_{R19-20}$, and FAM21$_{R20-21}$, were coned into pGEX4T2 vector for expression as a thrombin-cleavable N-terminal GST fusion protein. All the mutant constructs were conducted using site-directed mutagenesis approach with custom designed primers. All DNA constructs were verified using DNA sequencing.

Protein expression and purification.

All the protein constructs in this study were expressed using BL21 (DE3) competent cells and induced by isopropyl-β-D-1-thiogalactoside (IPTG) approach. In all cases unless noted otherwise, the cells were cultivated in Ultra Yield™ flasks at 37˚C and 180 rpm until the cell density reached OD_{600} ~0.8. A final concentration of 0.8 mM IPTG was then added to the expression culture and further incubated for 16 h to 18 h at 20˚C. To achieve the optimal expression yield of hSNX27$_{FERM}$, a final concentration of 0.5 mM IPTG was added to the culture prior to the incubation at 20˚C. After expression, the cells were pelleted and harvested by 10 min of centrifugation using JLA 8.1 rotor at 6000 rpm, 4˚C. The cell pellets were either stored at -80˚C or immediately proceeded to purification.

Purification of Retromer was performed using the protocol described previously (Chen *et al.*, 2021). In brief, the GST-tagged VPS29 co-expressed with VPS35 were mixed with the cell pellet of VPS26A. Cells were lysed through a Constant System TS-series high pressure cell disruptor in lysis buffer containing 50 mM Tris-HCl pH 7.5, 200 mM NaCl, 2 mM 2-Mercaptoethanol (β-ME), 1 mM benzamidine, 10 µg/mL

deoxyribonuclease I (DNase I). The soluble homogenate cleared by centrifugation was loaded onto Talon resin (Clonetech) followed by glutathione Sepharose (GE Healthcare) to obtain the correct stoichiometry ratio of the Retromer complex. For the VPS29 – $VPS35_{481-796}$ subcomplex and VPS29 alone, the purification was carried out using glutathione Sepharose (GE Healthcare) directly. Removal of the fusion tag from Retromer, subcomplex and VPS29 were performed using on-column cleavage with thrombin protease (Sigma-Aldrich) overnight at 4˚C. The flow-through containing the fusion tag free protein was further purified using size-exclusion chromatography (SEC) on a HiLoad® 16/600 Superdex 200 or Superdex 75 column equilibrated with buffer containing 50 mM Tris-HCl pH 7.5, 200 mM NaCl, 2 mM β-ME. Purification of hSNX27 constructs were carried our using protocol described previously (Simonetti *et al.*, 2022). For the FAM21 constructs, the cell pellet of GST-tagged FAM21 protein was resuspended in lysis buffer containing 20 mM Tris-HCl pH 7.5, 200 mM NaCl, 5% glycerol, 2 mM β-ME, 1 mM benzamidine, and 10 μg/mL DNase I. Cells were lysed and centrifuged using the same protocol as Retromer and SNX27. Supernatants of GST-tagged protein homogenates were loaded onto glutathione Sepharose™ beads (GE healthcare). Prior to the elution, the protein-bound bead was washed with 100 ml of washing buffer containing 20 mM Tris-HCl pH 7.5, 200 mM NaCl, 2 mM β-ME. The elution buffer then carried out using the same buffer as the washing buffer supplemented with freshly prepared 20 mM reduced glutathione and the 1 X cOmplete™ EDTA-free protease inhibitor tablet. The protease inhibitor table was added to protect the GST-tag from non-specific cleavage during purification. The SEC was performed as the final purification step using HiLoad® 16/600 Superdex 200 or Superdex 75 (GE Healthcare) column pre-equilibrated with buffer containing 50 mM Tris-HCl pH 7.5, 200 mM NaCl, 2 mM β-ME. Protein integrity was validated using SDS-PAGE gel and concentration was measured using Nanodrop at $OD_{280.}$

Isothermal titration calorimetry (ITC)

All microcalorimetry experiments were carried out at 25˚C using a PEAQ ITC (Malvern, UK) in SEC buffer. The interaction of Retromer and FAM21 peptides was carried out by titrating 400 - 600 μM of FAM21 peptides into 15 - 20 μM of Retromer, VPS29 – $VPS35_{481-796}$ subcomplex or VPS29. The effect of the cyclic peptide was performed by titrating 400 μM of FAM21 R21 peptides into 15 μM of VPS29 supplemented with 2 mM RT-D1. In the native control, the cyclic peptide was substituted with equivalent percentage (v/v) of DMSO. For the Retromer mutant experiment, 400 – 600 μM of GST-$FAM21_{R19-R20}$ or 600 μM of FAM21 R21 peptide was titrated into either 15 - 20 μM of native Retromer or $Retromer_{K555N, K556L, K559Q}$ mutant. In the case of SNX27 and FAM21 interaction, 300 μM of GST-$FAM21_{R19-21}$ was titrated into 12 μM of either $hSNX27_{FL}$ or $hSNX27_{FERM}$. For the binding tests of FAM21 peptides to SNX27, 800 μM of the FAM21 peptides were titrated into 20 μM $hSNX27_{FL}$ or $hSNX27_{FERM}$ proteins. Mutant binding experiment was performed by titrating 600 μM of $FAM21_{R19}$ peptide into 20 μM of either native or single point mutant form of $hSNX27_{FL}$.

All ITC experiments were performed with a single injection of 0.4 μL followed by a series of 12 injections of 3.2 μL each, spaced 180 seconds apart, and stirred at 850 rpm. By integrating the observed peaks and subtracting the heats of dilution from the background, the heat exchange of interactions was

calculated. The thermodynamic parameters Kd, ΔH, ΔG, and −TΔS for all binding tests were obtained by fitting and normalising data to a single-site binding model using the Malvern software package. The stoichiometry was adjusted initially, and if the value was nearly 1, N was set to exactly 1.0 for computation. To ensure the data were reproducible, each experiment was run at least twice.

Crystallisation

Crystallization screening was carried out using the hanging-drop vapour diffusion method at a temperature of 20˚C. To obtain the FAM21 R20 bound co-crystal structure, the purified VPS29 – $VPS35_{481-796}$ subcomplex was mixed with 8 molar excesses of $FAM21_{R20}$ peptide solubilized in 1 M HEPES pH 7.5. Crystals were observed in multiple different commercial screen conditions. Best diffracting quality crystals were obtained using streak seeding approach in 24-well plate with a final protein concentration of 10 mg/ml under condition comprising 0.1 M Sodium Citrate pH 4.2, 0.2 M NaCl 16% PEG1000. Rod shape crystals appeared after 1 day and grew to optimal after 5 days incubation at 20˚C. In the case of FAM21 R21 bound co-crystal structure, two different protein complexes were prepared. In the first case, the purified VPS29 – $VPS35_{481-796}$ subcomplex was mixed with 5 molar excesses of $FAM21_{R21}$ peptide solubilized in 1 M HEPES pH 7.5 at a final concentration of 12 mg/ml in condition containing 0.1 M MES pH 6.5, 0.1 M Magnesium Acetate, 10% PEG10,000. Crystals appeared after 3 days of incubation at 20˚C. In the second case, the purified VPS29 was mixed with 2 molar excesses of $FAM21_{R21}$ peptide at a final protein concentration of 15 mg/ml. The protein-$FAM21_{R21}$ peptide complex crystals were obtained in condition composed of 0.2 M Magnesium Formate, 20% PEG3350. Crystals appeared after 2 weeks of incubation at 20˚C.

To co-crystallize $hSNX27_{FERM}$ with FAM21 peptides, five-fold molar excesses of the $FAM21_{R15}$, $FAM21_{R19}$ and $FAM21_{R20}$ peptides were added respectively to the purified $hSNX27_{FERM}$ to a final concentration of 17 mg/ml. Additionally, 10 mM DTT was supplemented to protect free cysteines. For co-crystallisation with peptide $FAM21_{R20}$, $hSNX27_{FERM}$ was buffer exchanged to buffer containing 20 mM Tris pH 7.5, 100 mM NaCl, 5% glycerol and 1 mM β-ME. Initial needle-shaped crystals were observed in the commercial screen condition ProPlex C11, which contains 0.1 M Sodium Cacodylate pH 6.5 and 25% PEG4000. The best diffraction-quality crystals were produced in 24-well plate under conditions comprising 0.1 M Sodium Cacodylate pH 6.0 and 22.5% PEG4000; 0.1 M Sodium Cacodylate pH 6.5 and 25% PEG3350; 0.1 M Sodium Cacodylate pH 6.5 and 22.5% PEG4000 for $hSNX27_{FERM}$-$FAM21_{R15}$, $hSNX27_{FERM}$-$FAM21_{R19}$ and $hSNX27_{FERM}$-$FAM21_{R20}$ complexes respectively.

Crystallographic data collection and structure determination

The X-ray diffraction data were collected at 100 K on the MX2 beamlines at the Australian Synchrotron. All the collected data were indexed and integrated by AutoXDS (Kabsch, 2010) and scaled using Aimless (Evans & Murshudov, 2013). Phase was solved by molecular replacement using Phaser (McCoy *et al*, 2007). Crystal structures of VPS29 – $VPS35_{481-796}$ – $FAM21_{R20}$ and VPS29 – $VPS35_{481-796}$ – $FAM21_{R21}$ were solved using Retromer subcomplex hVPS29 – $hVPS35_{483-780}$ (PDB ID: 2R17) as the initial model. In the case of VPS29 – $FAM21_{R21}$ complex, human VPS29 from Vps29 – RT-D2 complex structure (PDB ID: 6XS7) was

used as the template. For hSNX27$_{FERM}$ – FAM21$_{R15}$, hSNX27$_{FERM}$ – FAM21$_{R19}$ and hSNX27$_{FERM}$ – FAM21$_{R20}$ complexes, the hSNX27$_{FERM}$ model generated by AlphaFold2 was used as the template. Structure refinement was performed using the PHENIX suite (Adams *et al*, 2010) with iterative rebuilding of the model. The refined model was manually rebuilded using Coot guided by Fo - Fc difference maps. Data collection and refinement statistics are summarized in **Supplementary Table S3**. Sequence conservation was based on a T-Coffee multiple sequence alignment (Notredame *et al*, 2000) and calculated using the ConSurf Server (Ashkenazy *et al*, 2016). Structural alignments and molecular figures were generated using PyMOL (Schrodinger, USA).

AlphaFold predictions of FAM21 peptides binding to hSNX27$_{FERM}$

We utilised the AlphaFold2 neural network (Jumper *et al*, 2021) of the open-source ColabFold pipeline (Mirdita *et al*, 2022) to produce models of FAM21 peptides that associate with Retromer or the SNX27 FERM domain. In the case of Retromer – FAM21 complex, the sequences of VPS29, VPS35 and FAM21 repeats 1, 2, 3, 4, 15, 16, 19, 20 and 21 were applied. For SNX27 – FAM21 complex, 12 of the acidic DLF motifs of the FAM21 were modelled with the sequence of the human SNX27 FERM domain (residues 271 to 528, NP_112180). The default settings for ColabFold were used to construct multiple sequence alignments using MMseqs2 (Mirdita *et al*, 2019) and perform structural relaxing of the final peptide geometry with Amber (Hornak *et al*, 2006), which resulted in the generation of three models for each peptide. Structural alignments and molecular figures were generated using PyMOL (Schrodinger, USA).

Antibodies

Antibodies used in this study were mouse monoclonal antibodies: GFP (clones 7.1 and 13.1; 11814460001; Roche, Germany) (1:2,000 for WB), DMT-1(sc-166884, Santa Cruz Biotechnology) (1:1,000 for WB), GADPH (97166, Cell Signaling Technologies) (1:1,000 for WB), ITGb1 (clone 18, BD610467, BD Biosciences) (1:1,000 for WB), N-Cadherin (13A9, Cell signaling technology) (1:1,000 for WB), SNX1 (clone 51/SNX1; 611482; BD, USA) (1:1,000 for WB), SNX2 (clone 13/SNX2; 5345661; BD) (1:1,000 for WB), SNX6 (clone d-5, 365965; Santa Cruz Biotechnology, USA) (1:1,000 for WB), SNX27 (ab77799, Abcam, UK) (1:1,000 for WB), β-actin (A1978; Sigma-Aldrich, USA) (1:2,000 for WB), VPS29 (clone d-1, 398874; Santa Cruz Biotechnology) (1:200 for WB), WASHC3 (clone B-10, sc-377146) (1:1,000 for WB); rabbit monoclonal antibodies: CI-MPR (EPR6599; 124767; Abcam) (1:1,000 for WB), VPS35 (EPR11501(B); 157220; Abcam) (1:1,000 for WB), GLUT1 (ab115730, Abcam) (1:1,000 for WB); rabbit polyclonal antibodies: FAM21 (kind gift from Dan Billadeau), KIDINS-220 (21856-1-AP, Proteintech) (1:1,000 for WB), LAT1 (5347S, Cell signaling technology) (1:1,000 for WB), GFP (GTX20290; GeneTex, USA) (WB 1:2,000), STEAP-3 (17186-1-AP, Proteintech) (1:1,000 for WB), VPS26A (23892; Abcam) (1:1,000 for WB), VPS35 (97545; Abcam) (1:1,000 for WB), VPS29 (98929; Abcam) (1:100 for WB), WASH1 (kind gift from Dan Billadeau) (1:1,000 for WB), WASHC5 (ABT69, Merck) (1:1,000 for WB).

Cell culture and transfection

527 HeLa, HEK-293T and H4 cell lines were sourced from and authenticated by ATCC. Cells were grown under
528 standard conditions in DMEM (Sigma-Aldrich) supplemented with 10% (v/v) FCS (Sigma-Aldrich) and 1%
529 penicillin/streptomycin (Gibco, USA). For GFP-based immunoprecipitations, HEK293T cells were
530 transfected with GFP constructs using polyethylenimine (Sigma-Aldrich) and expression was allowed for 24-
531 48 hours.
532
533 **Biotinylation of cell surface proteins**
534 For surface biotinylation experiments, fresh Sulfo-NHS-SS Biotin (Thermo Fisher Scientific, #21217) was
535 dissolved in ice-cold PBS at pH 7.8 at a final concentration of 0.2 mg/ml. Cells were washed twice in ice-
536 cold PBS and placed on ice to slow down the endocytic pathway. Next, cells were incubated with the
537 biotinylation reagent for 30 minutes at 4˚C followed by incubation in TBS for 10 minutes to quench the
538 unbound biotin. The cells were then lysed in lysis buffer and equal amounts of their proteins were subjected
539 to Streptavidin beads-based affinity isolation (GE Healthcare, USA).
540
541 **Immunoprecipitation and quantitative western blot analysis**
542 For western blotting, cells were lysed in PBS with 1% (v/v) Triton X-100 and Pierce protease inhibitor
543 cocktail (Thermo Scientific). The protein concentration was determined with a BCA assay kit (Thermo
544 Fisher Scientific, USA), and equal amounts were resolved on NuPAGE 4% to 12% precast gels (Invitrogen,
545 USA). Blotting was performed onto polyvinylidene difluoride membranes (Immobilon-FL; EMD Millipore,
546 USA) followed by detection using the Odyssey infrared scanning system (LI-COR Biosciences, USA). For
547 GFP-based immunoprecipitations, HEK-293T cells were lysed 48 hours after transfection in
548 immunoprecipitation buffer (50 mM Tris-HCl, 0.5% (v/v) NP-40, and Roche protease inhibitor cocktail) and
549 subjected to GFP trap (ChromoTek, Germany). Immunoblotting was performed using standard procedures.
550 Detection was performed on an Odyssey infrared scanning system (LI-COR Biosciences) using fluorescently
551 labeled secondary antibodies.
552
553 **TMT-labelling, Nano LC-MS/MS and Proteomic data analysis**
554 Were performed as described previously (Simonetti et al., 2019; Healy et al., 2023).
555

ACKNOWLEDGEMENTS:

We acknowledge use of the University of Queensland Remote Operation Crystallization and X-ray (UQ ROCX) Facility and the assistance of G.King and K.A.Arachchige. X-ray data were collected on the MX1 and MX2 microfocus beamline at the Australian Synchrotron. B.M.C. is supported by an Investigator Grant Project Grant from the National Health and Medical Research Council (APP2016410 and APP1156493). We thank the Bristol Proteomics Facility at the University of Bristol. P.J.C. is supported by the Wellcome Trust (104568/Z/14/Z amd 220260/Z/20/Z), the MRC (MR/L007363/1 and MR/P018807/1), the Lister Institute of Preventive Medicine, and the Royal Society Noreen Murray Research Professorship (RSRP/R1/211004). A.P.J. was funded through an MRC PhD Studentship.

AUTHOR CONTRIBUTIONS:

Initial Concept: B.M.C., and P.J.C.

Concept development: all authors.

ITC and structural determination and analysis: Q.G. and K.C.

Biochemistry and cell biology analysis: M.G-A., A.P.J., B.S., and C.M.D.

Proteomic analysis: K.J.H.

Data analysis and Figure generation: Q.G., K.C., A.P.J., B.S., and M.G-A.

Funding acquisition: B.M.C., and P.J.C.

Supervision: B.M.C., and P.J.C.

Writing – 1st draft: Q.G. and K.C.

(Writing – review & editing: all authors)

CONFLICTS OF INTEREST:

The authors declare that they have no conflict of interest.

FIGURES

Figure 1. Retromer VPS29 is responsible for binding to repeat 21 of FAM21.

(**A**) Schematic diagram showing features of human FAM21, and highlighting the 21 LFa repeats in the unstructured tail. (**B**) Sequences of the 21 LFa repeats within the FAM21 tail. Conserved [I/L]F residues are shown in grey and acidic residues are in red. The PL residues of repeat 21 are highlighted in green. (**C**) ITC thermograms showing the titration of Retromer, the VPS29–VPS35$_{481\text{-}796}$ subcomplex, and VPS29 alone with FAM21$_{R19}$ (blue); FAM21$_{R20}$ (green); and FAM21$_{R21}$ (red) peptides. (**D**) Retromer shows binding to GST-FAM21$_{R19\text{-}R20}$. (**E**) VPS29 and FAM21$_{R21}$ peptide interaction can be blocked by the addition of the PL-sequence containing cyclic peptide RT-D1. All ITC graphs show the integrated (bottom) and normalized raw data (top) fit with a single-site binding model.

Figure 2. Structural basis for the interaction of LFa repeats with Retromer subunit VPS35.

(**A**) Overall crystal structure of VPS29–VPS35$_{481\text{-}796}$ in complex with FAM21$_{R20}$ peptides showing both complexes from the asymmetric unit. (**B**) VPS35 is highly conserved in the FAM21$_{R20}$ binding region. The density corresponding to the FAM21$_{R20}$ peptide is shown in mesh using 2Fo–Fc map contoured at 1σ. Sequence conservation of VPS35 was mapped with CONSURF (Ashkenazy *et al.*, 2016). (**C**) The electrostatic surface map showing FAM21$_{R20}$ binding location on VPS35. (**D**) Predicted alignment Error (PAE) plots of VPS29–VPS35$_{481\text{-}796}$–FAM21$_{R19\text{-}R20}$ complexes generated by Alphafold2. (**E**) The predicted structure highlighting the per-residue confidence score (pLDDT) between 0 to 100. Regions showing low pLDDT score (green and orange) are likely to be unstructured. (**F**) Alignment of the Alphafold2 model of FAM21$_{R20}$ (cyan) and the crystal structure (VPS35 in light purple, FAM21$_{R20}$ as light pink) highlighting the key interacting residues between FAM21$_{R20}$ and VPS35. The insert shows the refined electron density of the FAM21$_{R20}$ peptide observed in the crystal structure. (**G**) Co-immunoprecipitation (co-IP) of C-terminal GFP-tagged VPS35mutants in the Site 2 binding pocket in HEK293T cells. (**H**) Co-IP of C-terminal GFP-tagged VPS35 and mutants in the Site 1 binding pocket. Quantitation of these Western blots is shown in **Figure S2.** (**I**) ITC analysis showing the binding of GST-FAM21$_{R19\text{-}R20}$ with either native Retromer or VPS35 (K555N/K556L/K559Q) Site 2 mutant. All ITC graphs show the integrated (bottom) and normalized raw data (top) fit with a single-site binding model. (**J**) The locations of the Site 1 and Site 2 FAM21 repeat binding sites are shown in the context of the VPS35-mediated Retromer dimer assembly derived from cryoelectron tomography (Leneva *et al.*, 2021). The location of the D620N mutation linked to Parkinson's Disease is also indicated in cyan spheres.

Figure 3. Structural basis for repeat 21 binding to VPS29 and model for Retromer engagement by multiple FAM21 repeats.

(**A**) Crystal structure of VPS29–VPS35$_{481\text{-}796}$ bound to the FAM21$_{R21}$ peptide. (**B**) Crystal structure of VPS29 in complex with FAM21$_{R21}$ peptide. (**C**) Enlarged view highlighting the refined density of FAM21$_{R21}$ peptide peptide (2Fo–Fc map contoured at 1σ). (**D**) Structural alignment of the VPS29–FAM21$_{R21}$ peptide complex with the VPS29–RT-D1 cyclic peptide complex (PDB ID 6XS5)(Chen *et al.*, 2021) highlighting the PL

motif binding region. (**E**) Predicted alignment Error (PAE) plots showing the predicted structure of VPS29–VPS35$_{481-796}$–FAM21$_{R19-R21}$ complex generated by Alphafold2. (**F**) The predicted structure highlighting the per-residue confidence score (pLDDT) between 0 to 100. Regions showing low pLDDT score (represents as green and orange) are likely to be unstructured. (**G**) Superimposition of all the two crystal structures with the Alphafold2 model. (**H**) Alphafold2 predictions of the complex of VPS29–VPS35 with either FAM21$_{R1-R2}$, FAM21$_{R3-R4}$ or FAM21$_{R15-R16}$ showing pairs of repeats predicted to bind to the same positively charged grooves as repeats FAM21$_{19-20}$. (**I**) ITC thermogram showing the binding between Retromer with FAM21$_{R5}$ (red line), FAM21$_{R15}$ (blue line) and FAM21$_{R17}$ (green) peptides. All ITC graphs show the integrated (right) and normalized raw data (left) fit with a single-site binding model. (**J**) The locations of the FAM21 repeat 19 and 20 binding sites as well as the VPS29-binding repeat 21 are shown in the context of the VPS35-mediated Retromer dimer assembly derived from cryoelectron tomography (Leneva *et al.*, 2021) (PDB ID: 7BLN). The right panel shows two proposed binding models for how FAM21 can bind to a Retromer dimer in *cis* or *trans*.

Figure 4. FAM21 aDLF repeats also binds to the SNX27 FERM domain.

(**A**) Co-IP of GFP-tagged FAM21 tail in HEK293T cells. Samples were analysed by quantitative fluorescence-based western blotting. The band intensities of SNX27 and VPS35 were measured from n=3 independent experiments using Odyssey software. The SNX27 and VPS35 band intensities, normalized to GFP expression, are presented as the average fraction of the full length FAM21 tail. (**B**) ITC analysis showing the binding between GST-FAM21$_{R19-21}$ and SNX27 (yellow line) and SNX27 FERM (blue line). (**C**) Similar binding experiment showing the binding of FAM21 peptides FAM21$_{R19}$, FAM21$_{R20}$ and FAM21$_{R21}$ with either (**C**) SNX27 FL or (**D**) SNX27 FERM. (**E**) ITC thermogram comparing the binding between native FAM21$_{R20}$ and ^{1298}IF^{1299} to SS mutant peptides with SNX27 FL. (**F**) List of FAM21 peptides containing the same aDLF motif to those observed in SNX1 and SNX2. (**G**) ITC binding curves of the FAM21$_{R5}$, FAM21$_{R8}$ and FAM21$_{R17}$ peptides titrated into either (**G**) SNX27 FL or (**H**) SNX27 FERM. All ITC graphs show the integrated (bottom) and normalized raw data (top) fit with a single-site binding model.

Figure 5. Structural basis for SNX27 interaction with FAM21 aDLF repeats.

(**A**) Crystal structures of the SNX27 FERM domain bound to aDLF repeats of FAM21. Top views show the key region of SNX27 FERM involved in the binding to the FAM21 aDLF seqeunces (**A**) FAM21$_{R15}$, (**B**) FAM21$_{R19}$ and (**C**) FAM21$_{R20}$. Middle panels show the electron density corresponding to a simulated-annealing composite omit 2Fo–Fc map contoured at 1σ. Bottom panels show electrostatic surface potential of SNX27 highlighting the positively charged pocket of SNX27 FERM. (**D**) Structural alignment showing the high degree of similarity between all three complex structures. (**E**) Sequence conservation map highlighting the conserved pocket of SNX27 FERM domain for binding to FAM21 aDLF motifs. (**F**) Structural alignment of SNX27 bound to FAM21$_{R19}$ with the SNX27–SNX1$_{75-92}$ complex (PDB ID 7CT1; (Yong *et al.*, 2021)) showing they bind the same pocket. (**G**) ITC analysis showing the binding of the FAM21$_{R19}$ peptide with the native or mutant forms of SNX27. The ITC graphs represent the integrated and

normalized data fit with 1:1 ratio binding. (**H**) Co-IP of GFP-SNX27 mutants and binding of WASH, Retromer and ESCPE-1 (represented by SNX6) proteins assessed by Western blot. (**I**) Proteomic studies comparing the native SNX27 and mutated SNX27 R498D binding capabilities with SNX27 interactors assessed by Co-IP (n = 6; derived from 2 biological repeats each with 3 technical repeats). Mutation of the aDLF binding pocket causes disrupted interactions with most WASH and ESCPE-1 subunits. The full list of detected proteins is provided in **Dataset S1**.

Figure 6. VPS35 interaction with FAM21 alone is not strictly required for SNX27–Retromer recycling. (A) VPS35 KO HeLa cells showed reduced cell surface levels of SNX27–Retromer dependent cargos including GLUT1 and KIDINS220. VPS35 KO clonal line was stably transduced with lentiviral particles containing VPS35-GFP WT or VPS35(K555N, K556L and K559Q), the mutation of the primary FAM21 binding Site 2. Re-expression and rescue with both constructs is able to rescue the cell surface levels of these cargos. This indicates that full binding of FAM21 to VPS35 is not strictly required for SNX27–Retromer mediated endosomal recycling. (B) Quantitation of Western blots is shown. Similar results were obtained in H4 cell lines as shown in **Figure S5C**.

Figure 7. Summary and proposed model for the cooperative recruitment of FAM21 by Retromer, SNX27 and other endosomal proteins.
The WASH subunit FAM21 has 21 LFa repeated elements in its extended tail that are rich in acidic, isoleucine and phenylalanine residues. LFa sequences possess two [L/I]F motifs interspersed by an acidic stretch ([L/I]F[D/E]$_{3\text{-}9}$[L/I]F). These bind two conserved sites towards the C-terminus of the VPS35 subunit of Retromer. The last repeated element of FAM21 has a specific PL dipeptide sequence that promotes interaction with Retromer subunit VPS29. This would be mutually exclusive of binding to other VPS29 interactors such as TBC1D5, ANKRD27, VPS35L and bacterial effector RidL. aDLF sequences are a subset of the LFa repeats with an acidic stretch prior to a D[L/I]F motif that associate with a conserved pocket in the SNX27 FERM domain, and are also found in the SNX1 and SNX2 proteins of the ESCPE-1 complex.

692 **SUPPLEMENTARY FIGURES AND DATA**

693 **Figure S1. Sequence alignment of FAM21/WASHC2 repeats 19, 20 and 21.**

694 Repeats 19-21 of FAM21 are aligned from various species. Conserved [I/L]F dipeptide motifs are indicated
695 by yellow arrows while the specific PL motif in repeat 21 is indivated by green ovals. h, homo sapiens; m,
696 Mus musculus; r, Rattus norvegicus; b, Bos taurus; d, Drosophila melanogaster; zf, Danio rerio.

697

698 **Figure S2. Quantitation of the Western blots shown in Figure 2G and 2H.**

699 Band intensities from **Figure 2G and 2H** were quantified using Odyssey software and normalized to GFP
700 expression. 1-way ANOVA with Dunnett's multiple comparisons test. Error bars represent the standard error.
701 *P < 0.05, **P < 0.01, ***P < 0.001, ****P < 0.0001.

702

703 **Figure S3. Alphafold models of VPS35–VPS29 in complex with different FAM21 LFa repeats.**

704 (**A**) Predicted alignment Error (PAE) plots for the AlphaFold2-predicted structures of the human (**A**)
705 VPS35–VPS29–FAM21$_{R1-R2}$ complex, (**B**) VPS35–VPS29–FAM21$_{R3-R4}$ complex, (**C**) VPS35–VPS29–
706 FAM21$_{R15-R16}$ complex. On the right the predicted structures are shown coloured according to the per-residue
707 confidence score (pLDDT) between 0 to 100. Regions showing a low pLDDT score (green and orange) are
708 likely to be unstructured.

709

710 **Figure S4. Alphafold models of SNX27 FERM domain in complex with various FAM21 aDLF**
711 **sequences.**

712 (**A**) Overlay of all AlphaFold2 predicted structures shown as Cα backbone ribbon. The sequences of the
713 aDLF repeats are shown in **Figure 4F.** (**B**) The predicted complex of SNX27$_{FERM}$ bound to FAM21 aDLF
714 sequence from repeat 1. SNX27 is shown in cartoon representation coloured according to pLDDT score. The
715 FAM21$_{R1}$ peptide is shown in green sticks. (**C**) Predicted alignment Error (PAE) plots showing the predicted
716 structure of human SNX27$_{FERM}$–FAM21 aDLF complexes. The top ranked prediction is shown in close up in
717 the left hand panels.

718

719 **Figure S5. Interactions of SNX27 and FAM21 mutants and VPS35 rescue experiments in H4 cells.**

720 (**A**) Co-IP of GFP-SNX27 wild-type and R498D mutant and binding of WASH, Retromer (indicated by
721 subunit VPS26A) and model cargo KIDINS220 assessed by Western blot. (**B**) Co-IP of GFP-FAM21 and
722 mutants shows that specific mutations in repeats 19-21 do not prevent binding to Retromer or SNX27 in cells.
723 KK is the combination of D1268K and D1297K mutants. (**C**) VPS35 KO H4 cells showed reduced cell
724 surface levels of SNX27–Retromer dependent cargos including CTR1, GLUT1 and KIDINS220. Re-
725 expression and rescue with both GFP-VPS35 wild-type protein and GFP-VPS35(K555N, K556L and K559Q)
726 with mutation of the FAM21 binding Site 1 is able to rescue the cell surface levels of these cargos. This
727 indicates that Site 2 in VPS35 is not strictly required for SNX27–Retromer mediated endosomal recycling.
728 Band intensities for all blots were quantified using Odyssey software and normalized to GFP expression. 1-

729 way ANOVA with Dunnett's multiple comparisons test. Error bars represent the mean, s.d. *P < 0.05, **P <
730 0.01, ***P < 0.001, ****P < 0.0001.
731
732 **Dataset S1. Proteomic interactions of GFP-SNX27(R498D) mutant versus GFP-SNX27 wild type.**
733

REFERENCES:

Adams PD, Afonine PV, Bunkoczi G, Chen VB, Davis IW, Echols N, Headd JJ, Hung LW, Kapral GJ, Grosse-Kunstleve RW *et al* (2010) PHENIX: a comprehensive Python-based system for macromolecular structure solution. *Acta Crystallogr D Biol Crystallogr* 66: 213-221

Ashkenazy H, Abadi S, Martz E, Chay O, Mayrose I, Pupko T, Ben-Tal N (2016) ConSurf 2016: an improved methodology to estimate and visualize evolutionary conservation in macromolecules. *Nucleic Acids Res* 44: W344-350

Balana B, Maslennikov I, Kwiatkowski W, Stern KM, Bahima L, Choe S, Slesinger PA (2011) Mechanism underlying selective regulation of G protein-gated inwardly rectifying potassium channels by the psychostimulant-sensitive sorting nexin 27. *Proc Natl Acad Sci U S A* 108: 5831-5836

Bartuzi P, Billadeau DD, Favier R, Rong S, Dekker D, Fedoseienko A, Fieten H, Wijers M, Levels JH, Huijkman N *et al* (2016) CCC- and WASH-mediated endosomal sorting of LDLR is required for normal clearance of circulating LDL. *Nat Commun* 7: 10961

Boesch DJ, Singla A, Han Y, Kramer DA, Liu Q, Suzuki K, Juneja P, Zhao X, Long X, Medlyn MJ *et al* (2023) Structural Organization of the Retriever-CCC Endosomal Recycling Complex. *bioRxiv*: 2023.2006.2006.543888

Buckley CM, Gopaldass N, Bosmani C, Johnston SA, Soldati T, Insall RH, King JS (2016) WASH drives early recycling from macropinosomes and phagosomes to maintain surface phagocytic receptors. *Proc Natl Acad Sci U S A* 113: E5906-E5915

Burd C, Cullen PJ (2014) Retromer: a master conductor of endosome sorting. *Cold Spring Harb Perspect Biol* 6

Burianek LE, Soderling SH (2013) Under lock and key: spatiotemporal regulation of WASP family proteins coordinates separate dynamic cellular processes. *Semin Cell Dev Biol* 24: 258-266

Chakrabarti R, Lee M, Higgs HN (2021) Multiple roles for actin in secretory and endocytic pathways. *Curr Biol* 31: R603-R618

Chen KE, Guo Q, Hill TA, Cui Y, Kendall AK, Yang Z, Hall RJ, Healy MD, Sacharz J, Norwood SJ *et al* (2021) De novo macrocyclic peptides for inhibiting, stabilizing, and probing the function of the retromer endosomal trafficking complex. *Sci Adv* 7: eabg4007

Chen KE, Healy MD, Collins BM (2019) Towards a molecular understanding of endosomal trafficking by Retromer and Retriever. *Traffic* 20: 465-478

Christie M, Chang CW, Rona G, Smith KM, Stewart AG, Takeda AA, Fontes MR, Stewart M, Vertessy BG, Forwood JK *et al* (2016) Structural Biology and Regulation of Protein Import into the Nucleus. *J Mol Biol* 428: 2060-2090

Clairfeuille T, Mas C, Chan AS, Yang Z, Tello-Lafoz M, Chandra M, Widagdo J, Kerr MC, Paul B, Merida I *et al* (2016) A molecular code for endosomal recycling of phosphorylated cargos by the SNX27-retromer complex. *Nat Struct Mol Biol* 23: 921-932

Crawley-Snowdon H, Yang JC, Zaccai NR, Davis LJ, Wartosch L, Herman EK, Bright NA, Swarbrick JS, Collins BM, Jackson LP *et al* (2020) Mechanism and evolution of the Zn-fingernail required for interaction of VARP with VPS29. *Nat Commun* 11: 5031

Cullen PJ, Steinberg F (2018) To degrade or not to degrade: mechanisms and significance of endocytic recycling. *Nat Rev Mol Cell Biol* 19: 679-696

de Bot ST, Vermeer S, Buijsman W, Heister A, Voorendt M, Verrips A, Scheffer H, Kremer HP, van de Warrenburg BP, Kamsteeg EJ (2013) Pure adult-onset spastic paraplegia caused by a novel mutation in the KIAA0196 (SPG8) gene. *J Neurol* 260: 1765-1769

Derivery E, Sousa C, Gautier JJ, Lombard B, Loew D, Gautreau A (2009) The Arp2/3 activator WASH controls the fission of endosomes through a large multiprotein complex. *Dev Cell* 17: 712-723

Dostál V, Humhalová T, Beránková P, Pácalt O, Libusová L (2022) SWIP mediates retromer-independent membrane recruitment of the WASH complex. *bioRxiv*: 2022.2008.2016.504073

Duleh SN, Welch MD (2010) WASH and the Arp2/3 complex regulate endosome shape and trafficking. *Cytoskeleton (Hoboken)* 67: 193-206

Evans PR, Murshudov GN (2013) How good are my data and what is the resolution? *Acta Crystallogr D Biol Crystallogr* 69: 1204-1214

Fokin AI, David V, Oguievetskaia K, Derivery E, Stone CE, Cao L, Rocques N, Molinie N, Henriot V, Aumont-Nicaise M *et al* (2021) The Arp1/11 minifilament of dynactin primes the endosomal Arp2/3 complex. *Sci Adv* 7

Fokin AI, Gautreau AM (2021) Assembly and Activity of the WASH Molecular Machine: Distinctive Features at the Crossroads of the Actin and Microtubule Cytoskeletons. *Front Cell Dev Biol* 9: 658865

Freeman CL, Hesketh G, Seaman MN (2014) RME-8 coordinates the activity of the WASH complex with the function of the retromer SNX dimer to control endosomal tubulation. *J Cell Sci* 127: 2053-2070

Gallon M, Clairfeuille T, Steinberg F, Mas C, Ghai R, Sessions RB, Teasdale RD, Collins BM, Cullen PJ (2014) A unique PDZ domain and arrestin-like fold interaction reveals mechanistic details of endocytic recycling by SNX27-retromer. *Proc Natl Acad Sci U S A* 111: E3604-3613

Ghai R, Mobli M, Norwood SJ, Bugarcic A, Teasdale RD, King GF, Collins BM (2011) Phox homology band 4.1/ezrin/radixin/moesin-like proteins function as molecular scaffolds that interact with cargo receptors and Ras GTPases. *Proc Natl Acad Sci U S A* 108: 7763-7768

Ghai R, Tello-Lafoz M, Norwood SJ, Yang Z, Clairfeuille T, Teasdale RD, Merida I, Collins BM (2015) Phosphoinositide binding by the SNX27 FERM domain regulates its localization at the immune synapse of activated T-cells. *J Cell Sci* 128: 553-565

Gomez TS, Billadeau DD (2009) A FAM21-containing WASH complex regulates retromer-dependent sorting. *Dev Cell* 17: 699-711

Gomez TS, Gorman JA, de Narvajas AA, Koenig AO, Billadeau DD (2012) Trafficking defects in WASH-knockout fibroblasts originate from collapsed endosomal and lysosomal networks. *Mol Biol Cell* 23: 3215-3228

Harbour ME, Breusegem SY, Antrobus R, Freeman C, Reid E, Seaman MN (2010) The cargo-selective retromer complex is a recruiting hub for protein complexes that regulate endosomal tubule dynamics. *J Cell Sci* 123: 3703-3717

Harbour ME, Breusegem SY, Seaman MN (2012) Recruitment of the endosomal WASH complex is mediated by the extended 'tail' of Fam21 binding to the retromer protein Vps35. *Biochem J* 442: 209-220

Healy MD, McNally KE, Butkovic R, Chilton M, Kato K, Sacharz J, McConville C, Moody ERR, Shaw S, Planelles-Herrero VJ *et al* (2023) Structure of the endosomal Commander complex linked to Ritscher-Schinzel syndrome. *Cell* 186: 2219-2237 e2229

Helfer E, Harbour ME, Henriot V, Lakisic G, Sousa-Blin C, Volceanov L, Seaman MNJ, Gautreau A (2013) Endosomal recruitment of the WASH complex: active sequences and mutations impairing interaction with the retromer. *Biol Cell* 105: 191-207

Hornak V, Abel R, Okur A, Strockbine B, Roitberg A, Simmerling C (2006) Comparison of multiple Amber force fields and development of improved protein backbone parameters. *Proteins* 65: 712-725

Huang W, Liu Z, Yang F, Zhou H, Yong X, Yang X, Zhou Y, Xue L, Zhang Y, Liu D *et al* (2019) Structural and functional studies of TBC1D23 C-terminal domain provide a link between endosomal trafficking and PCH. *Proc Natl Acad Sci U S A* 116: 22598-22608

Jia D, Gomez TS, Billadeau DD, Rosen MK (2012) Multiple repeat elements within the FAM21 tail link the WASH actin regulatory complex to the retromer. *Mol Biol Cell* 23: 2352-2361

Jia D, Gomez TS, Metlagel Z, Umetani J, Otwinowski Z, Rosen MK, Billadeau DD (2010) WASH and WAVE actin regulators of the Wiskott-Aldrich syndrome protein (WASP) family are controlled by analogous structurally related complexes. *Proc Natl Acad Sci U S A* 107: 10442-10447

Jia D, Zhang JS, Li F, Wang J, Deng Z, White MA, Osborne DG, Phillips-Krawczak C, Gomez TS, Li H *et al* (2016) Structural and mechanistic insights into regulation of the retromer coat by TBC1d5. *Nat Commun* 7: 13305

Jumper J, Evans R, Pritzel A, Green T, Figurnov M, Ronneberger O, Tunyasuvunakool K, Bates R, Zidek A, Potapenko A *et al* (2021) Highly accurate protein structure prediction with AlphaFold. *Nature* 596: 583-589

Kabsch W (2010) Xds. *Acta Crystallogr D Biol Crystallogr* 66: 125-132

Kovtun O, Leneva N, Bykov YS, Ariotti N, Teasdale RD, Schaffer M, Engel BD, Owen DJ, Briggs JAG, Collins BM (2018) Structure of the membrane-assembled retromer coat determined by cryo-electron tomography. *Nature* 561: 561-564

Kvainickas A, Orgaz AJ, Nagele H, Diedrich B, Heesom KJ, Dengjel J, Cullen PJ, Steinberg F (2017) Retromer- and WASH-dependent sorting of nutrient transporters requires a multivalent interaction network with ANKRD50. *J Cell Sci* 130: 382-395

Laulumaa S, Kumpula E-P, Huiskonen JT, Varjosalo M (2023) Structure and Interactions of the Endogenous Human Commander Complex. *bioRxiv*: 2023.2004.2003.535349

Lee S, Chang J, Blackstone C (2016) FAM21 directs SNX27-retromer cargoes to the plasma membrane by preventing transport to the Golgi apparatus. *Nat Commun* 7: 10939

Leneva N, Kovtun O, Morado DR, Briggs JAG, Owen DJ (2021) Architecture and mechanism of metazoan retromer:SNX3 tubular coat assembly. *Sci Adv* 7

Li Y, Liao S, Li F, Zhu Z (2019) Crystal Structure of the PX Domain of SNX27. *Biochemistry (Mosc)* 84: 147-152

Liu N, Liu K, Yang C (2022) WDR91 specifies the endosomal retrieval subdomain for retromer-dependent recycling. *J Cell Biol* 221

McCoy AJ, Grosse-Kunstleve RW, Adams PD, Winn MD, Storoni LC, Read RJ (2007) Phaser crystallographic software. *J Appl Crystallogr* 40: 658-674

McGough IJ, Steinberg F, Gallon M, Yatsu A, Ohbayashi N, Heesom KJ, Fukuda M, Cullen PJ (2014a) Identification of molecular heterogeneity in SNX27-retromer-mediated endosome-to-plasma-membrane recycling. *J Cell Sci* 127: 4940-4953

McGough IJ, Steinberg F, Jia D, Barbuti PA, McMillan KJ, Heesom KJ, Whone AL, Caldwell MA, Billadeau DD, Rosen MK *et al* (2014b) Retromer binding to FAM21 and the WASH complex is perturbed by the Parkinson disease-linked VPS35(D620N) mutation. *Curr Biol* 24: 1670-1676

McNally KE, Faulkner R, Steinberg F, Gallon M, Ghai R, Pim D, Langton P, Pearson N, Danson CM, Nagele H *et al* (2017) Retriever is a multiprotein complex for retromer-independent endosomal cargo recycling. *Nat Cell Biol* 19: 1214-1225

Miller HE, Larson CL, Heinzen RA (2018) Actin polymerization in the endosomal pathway, but not on the Coxiella-containing vacuole, is essential for pathogen growth. *PLoS Pathog* 14: e1007005

Mirdita M, Schutze K, Moriwaki Y, Heo L, Ovchinnikov S, Steinegger M (2022) ColabFold: making protein folding accessible to all. *Nat Methods* 19: 679-682

Mirdita M, Steinegger M, Soding J (2019) MMseqs2 desktop and local web server app for fast, interactive sequence searches. *Bioinformatics* 35: 2856-2858

Notredame C, Higgins DG, Heringa J (2000) T-Coffee: A novel method for fast and accurate multiple sequence alignment. *J Mol Biol* 302: 205-217

Padrick SB, Rosen MK (2010) Physical mechanisms of signal integration by WASP family proteins. *Annu Rev Biochem* 79: 707-735

Park M, Kim HJ, Lim B, Wylegala A, Toborek M (2013) Methamphetamine-induced occludin endocytosis is mediated by the Arp2/3 complex-regulated actin rearrangement. *J Biol Chem* 288: 33324-33334

Phillips-Krawczak CA, Singla A, Starokadomskyy P, Deng Z, Osborne DG, Li H, Dick CJ, Gomez TS, Koenecke M, Zhang JS *et al* (2015) COMMD1 is linked to the WASH complex and regulates endosomal trafficking of the copper transporter ATP7A. *Mol Biol Cell* 26: 91-103

Romano-Moreno M, Rojas AL, Williamson CD, Gershlick DC, Lucas M, Isupov MN, Bonifacino JS, Machner MP, Hierro A (2017) Molecular mechanism for the subversion of the retromer coat by the Legionella effector RidL. *Proc Natl Acad Sci U S A* 114: E11151-E11160

Ropers F, Derivery E, Hu H, Garshasbi M, Karbasiyan M, Herold M, Nurnberg G, Ullmann R, Gautreau A, Sperling K *et al* (2011) Identification of a novel candidate gene for non-syndromic autosomal recessive intellectual disability: the WASH complex member SWIP. *Hum Mol Genet* 20: 2585-2590

Ryder PV, Vistein R, Gokhale A, Seaman MN, Puthenveedu MA, Faundez V (2013) The WASH complex, an endosomal Arp2/3 activator, interacts with the Hermansky-Pudlak syndrome complex BLOC-1 and its cargo phosphatidylinositol-4-kinase type IIalpha. *Mol Biol Cell* 24: 2269-2284

Schmid EM, McMahon HT (2007) Integrating molecular and network biology to decode endocytosis. *Nature* 448: 883-888

Seaman MN, Gautreau A, Billadeau DD (2013) Retromer-mediated endosomal protein sorting: all WASHed up! *Trends Cell Biol* 23: 522-528

Seaman MN, Harbour ME, Tattersall D, Read E, Bright N (2009) Membrane recruitment of the cargo-selective retromer subcomplex is catalysed by the small GTPase Rab7 and inhibited by the Rab-GAP TBC1D5. *J Cell Sci* 122: 2371-2382

Seaman MNJ, Mukadam AS, Breusegem SY (2018) Inhibition of TBC1D5 activates Rab7a and can enhance the function of the retromer cargo-selective complex. *J Cell Sci* 131

Shin JJH, Gillingham AK, Begum F, Chadwick J, Munro S (2017) TBC1D23 is a bridging factor for endosomal vesicle capture by golgins at the trans-Golgi. *Nat Cell Biol* 19: 1424-1432

Simonetti B, Cullen PJ (2019) Actin-dependent endosomal receptor recycling. *Curr Opin Cell Biol* 56: 22-33

Simonetti B, Guo Q, Gimenez-Andres M, Chen KE, Moody ERR, Evans AJ, Chandra M, Danson CM, Williams TA, Collins BM *et al* (2022) SNX27-Retromer directly binds ESCPE-1 to transfer cargo proteins during endosomal recycling. *PLoS Biol* 20: e3001601

Singla A, Fedoseienko A, Giridharan SSP, Overlee BL, Lopez A, Jia D, Song J, Huff-Hardy K, Weisman L, Burstein E *et al* (2019) Endosomal PI(3)P regulation by the COMMD/CCDC22/CCDC93 (CCC) complex controls membrane protein recycling. *Nat Commun* 10: 4271

Steinberg F, Gallon M, Winfield M, Thomas EC, Bell AJ, Heesom KJ, Tavare JM, Cullen PJ (2013) A global analysis of SNX27-retromer assembly and cargo specificity reveals a function in glucose and metal ion transport. *Nat Cell Biol* 15: 461-471

Teilum K, Olsen JG, Kragelund BB (2021) On the specificity of protein-protein interactions in the context of disorder. *Biochem J* 478: 2035-2050

Temkin P, Lauffer B, Jager S, Cimermancic P, Krogan NJ, von Zastrow M (2011) SNX27 mediates retromer tubule entry and endosome-to-plasma membrane trafficking of signalling receptors. *Nat Cell Biol* 13: 715-721

Valdmanis PN, Meijer IA, Reynolds A, Lei A, MacLeod P, Schlesinger D, Zatz M, Reid E, Dion PA, Drapeau P *et al* (2007) Mutations in the KIAA0196 gene at the SPG8 locus cause hereditary spastic paraplegia. *Am J Hum Genet* 80: 152-161

Vardarajan BN, Bruesegem SY, Harbour ME, Inzelberg R, Friedland R, St George-Hyslop P, Seaman MN, Farrer LA (2012) Identification of Alzheimer disease-associated variants in genes that regulate retromer function. *Neurobiol Aging* 33: 2231 e2215-2231 e2230

Yong X, Zhao L, Hu W, Sun Q, Ham H, Liu Z, Ren J, Zhang Z, Zhou Y, Yang Q *et al* (2021) SNX27-FERM-SNX1 complex structure rationalizes divergent trafficking pathways by SNX17 and SNX27. *Proc Natl Acad Sci U S A* 118

Zavodszky E, Seaman MN, Moreau K, Jimenez-Sanchez M, Breusegem SY, Harbour ME, Rubinsztein DC (2014) Mutation in VPS35 associated with Parkinson's disease impairs WASH complex association and inhibits autophagy. *Nat Commun* 5: 3828

948 **SUPPLEMENTARY MATERIALS:**

949

950 **Table S1. Thermodynamic parameters for the binding of FAM21 with Retromer by ITC**

951

Syringe	Cell	K_d (nM)	ΔH (kcal/mol)	ΔG (kcal/mol)	$-T\Delta S$ (kcal/mol)
		FAM21 peptides against Retromer			
$FAM21_{R19}$	Retromer	63.5 ± 8.7	-1.2 ± 0.2	-5.7 ± 0.1	-4.5 ± 0.3
$FAM21_{R20}$	Retromer		N.B.		
$FAM21_{R21}$	Retromer	26.8 ± 4.3	-2.8 ± 0.6	-6.2 ± 0.1	-3.4 ± 0.7
		FAM21 peptides against mVps29 – $mVps35_{481-796}$			
$FAM21_{R19}$	mVps29 – $mVps35_{481-796}$	61.1 ± 6.4	-1.9 ± 1.4	-5.8 ± 0.1	-3.8 ± 1.3
$FAM21_{R20}$	mVps29 – $mVps35_{481-796}$		N.B.		
$FAM21_{R21}$	mVps29 – $mVps35_{481-796}$	31.4 ± 1.1	-2.6 ± 1.0	-6.2 ± 0.1	-3.6 ± 1.2
		FAM21 peptides against mVps29			
$FAM21_{R19}$	mVps29		N.B.		
$FAM21_{R20}$	mVps29		N.B.		
$FAM21_{R21}$	mVps29	26.6 ± 2.6	-2.9 ± 0.1	-6.3 ± 0.1	-3.4 ± 0.2

952

953

Table S2. Summary of crystallographic structure determination statistics of Retromer subcomplex with FAM21 repeats.

Data collection statistics	mVPS29 - mVPS35$_{481-796}$ - FAM21$_{R20}$	mVPS29 - mVPS35$_{481-796}$ - FAM21$_{R21}$	mVPS29 - FAM21$_{R21}$
PDB ID	8TTC	8TTA	8TTD
Space group	$P4_32_12$	C121	$P3_221$
Resolution (Å)	46.90 - 3.01 (3.20 - 3.01)	49.31 - 3.46 (3.79 - 3.46)	41.28 - 2.01 (2.06 - 2.01)
a, b, c (Å)	88.76, 88.76, 328.29	123.73, 165.58, 68.00	43.34, 43.34, 165.14
α, β, γ (°)	90.00 90.00 90.00	90.00, 117.51, 90.00	90.00, 90.00, 120.00
Total observations	348,827 (54,935)	110,783 (26,173)	239,643 (17,499)
Unique reflections	27,047 (4,201)	15,793 (3,693)	12,765 (911)
Completeness (%)	99.6 (97.9)	99.3 (97.6)	99.9 (99.0)
R_{merge}[+]	0.137 (1.588)	0.342 (1.233)	0.052 (0.475)
R_{pim}*	0.040 (0.451)	0.139 (0.494)	0.016 (0.152)
CC1/2	0.998 (0.812)	0.993 (0.762)	1.000 (0.972)
$\langle I/\sigma(I)\rangle$	11.7 (1.3)	4.5 (1.3)	25.4 (4.5)
Multiplicity	12.9 (13.1)	7.0 (7.1)	18.8 (19.2)
Molecule/asym	2	2	1
Refinement statistics			
R_{work}/R_{free} (%) [¶#]	24.90/27.40	22.22/25.39	18.81/24.41
No. protein atoms	7747	7908	1507
Waters	17	10	26
Wilson B (Å^2)	90.59	77.56	42.24
Average B (Å^2)^	101.87	83.95	59.45
Protein	102.13	84.00	59.53
ligands	63.10	85.78	96.35
Water	83.53	41.92	50.70
rmsd bonds (Å)	0.006	0.006	0.007
rmsd angles (°)	1.11	1.08	1.08
Ramachandran plot: Favored/outliers (%)	93.28/1.37	93.42/0.93	94.02/0.54

Values in parentheses refer to the highest resolution shell. [+]$R_{merge} = \Sigma|I - \langle I\rangle| / \Sigma\langle I\rangle$, where I is the intensity of each individual reflection. *R_{pim} indicates all I^+ & I^-. [¶]$R_{work} = \Sigma h|F_o - F_c|/ \Sigma_l| F_o|$, where F_o *and* F_c are the observed and calculated structure-factor amplitudes for each reflection h. [#]R_{free} was calculated with 10% of the diffraction data selected randomly and excluded from refinement. ^Calculated using Baverage.

962 **Table S3. Thermodynamic parameters for the binding of FAM21 with SNX27 by ITC**

963

Syringe	Cell	K_d (μM)	ΔH (kcal/mol)	ΔG (kcal/mol)	$-T\Delta S$ (kcal/mol)
FAM21 $_{R19-21}$ against SNX27 proteins					
$FAM21_{R19-21}$	$hSNX27_{FL}$	5.70 ± 1.94	-1.51 ± 0.45	-7.18 ± 0.21	-5.67 ± 0.25
$FAM21_{R19-21}$	$hSNX27_{FERM}$	4.97 ± 1.32	-2.50 ± 0.25	-7.25 ± 0.16	-4.75 ± 0.41
FAM21 peptides against $hSNX27_{FL}$					
$FAM21_{R5}$	$hSNX27_{FL}$	23.55 ± 2.19	-1.28 ± 0.15	-6.32 ± 0.05	-5.04 ± 0.10
$FAM21_{R8}$	$hSNX27_{FL}$	68.80 ± 1.27	-2.12 ± 0.04	-5.69 ± 0.01	-3.57 ± 0.05
$FAM21_{R17}$	$hSNX27_{FL}$	70.55 ± 0.64	-2.10 ± 0.57	-5.67 ± 0.01	-3.57 ± 0.58
$FAM21_{R19}$	$hSNX27_{FL}$	6.96 ± 0.12	-2.22 ± 0.17	-7.04 ± 0.01	-4.82 ± 0.18
$FAM21_{R20}$	$hSNX27_{FL}$	19.00 ± 0.28	-1.70 ± 0.28	-6.45 ± 0.01	-4.75 ± 0.29
$FAM21_{R20}$ mutant	$hSNX27_{FL}$	No binding detected			
$FAM21_{R21}$	$hSNX27_{FL}$	No binding detected			
FAM21 peptides against $hSNX27_{FERM}$					
$FAM21_{R5}$	$hSNX27_{FERM}$	29.20 ± 0.28	-3.05 ± 0.62	-6.19 ± 0.01	-3.14 ± 0.61
$FAM21_{R8}$	$hSNX27_{FERM}$	42.50 ± 2.97	-2.87 ± 0.19	-5.97 ± 0.04	-3.11 ± 0.23
$FAM21_{R17}$	$hSNX27_{FERM}$	31.70 ± 0.57	-3.11 ± 0.92	-6.14 ± 0.01	-3.03 ± 0.93
$FAM21_{R19}$	$hSNX27_{FERM}$	38.35 ± 1.34	-3.33 ± 0.52	-6.03 ± 0.02	-2.70 ± 0.49
$FAM21_{R20}$	$hSNX27_{FERM}$	25.55 ± 0.35	-3.00 ± 0.29	-6.27 ± 0.01	-3.27 ± 0.28
$FAM21_{R21}$	$hSNX27_{FERM}$	No binding detected			
$FAM21_{R19}$ peptide against $hSNX27_{FL}$ mutants					
$FAM21_{R19}$	$hSNX27_{FL}$ R437D	No binding detected			
$FAM21_{R19}$	$hSNX27_{FL}$ K495D	58.30 ± 1.41	-2.33 ± 0.34	-5.78 ± 0.01	-3.45 ± 0.35
$FAM21_{R19}$	$hSNX27_{FL}$ K496D	33.53 ± 1.48	-2.97 ± 1.53	-4.99 ± 1.96	-3.14 ± 1.52
$FAM21_{R19}$	$hSNX27_{FL}$ R498D	No binding detected			
$FAM21_{R19}$	$hSNX27_{FL}$ K501D	38.80 ± 0.28	-2.14 ± 0.95	-6.02 ± 0.00	-3.88 ± 0.95

964

965

966

967

Table S4. Summary of crystallographic structure determination statistics for $SNX27_{FERM}$ and FAM21 repeats.

Data collection statistics	$hSNX27_{FERM}$ - $FAM21_{R15}$	$hSNX27_{FERM}$ - $FAM21_{R19}$	$hSNX27_{FERM}$ - $FAM21_{R20}$
PDB ID	8TTT	8TTU	8TTV
Space group	$P2_12_12_1$	$P2_12_12_1$	$P2_12_12_1$
Resolution (Å)	42.95– 2.33	37.54 – 2.36	42.91 – 2.00
	(2.41 – 2.33)	(2.45 – 2.36)	(2.05 – 2.00)
a, b, c (Å)	37.57, 74.37, 105.23 90.00,	37.54, 74.50, 102.53	37.97, 74.20, 105.19
α, β, γ (°)	90.00, 90.00	90.0, 90.0, 90.0	90.0, 90.0, 90.0
Total observations	88510 (5906)	64599 (6238)	139518 (8637)
Unique reflections	12909 (940)	12319 (1195)	20806 (1385)
Completeness (%)	97.6 (75.9)	98.8 (93.5)	99.5 (94.2)
R_{merge} [+]	0.203 (1.524)	0.097 (0.545)	0.240 (2.161)
R_{pim*}	0.083 (0.632)	0.048 (0.263)	0.101 (0.943)
CC1/2	0.995 (0.379)	0.995 (0.801)	0.989 (0.205)
$<I/\sigma(I)>$	7.9 (1.1)	8.4 (1.7)	6.7 (1.0)
Multiplicity	6.9 (6.3)	5.2 (5.2)	6.7 (6.2)
Molecule/asymmetry	1	1	1
Refinement statistics			
R_{work}/R_{free} (%) [¶#]	19.05/25.04	20.04/25.26	20.64/26.38
No. protein atoms	2187	2192	2184
Waters	45	28	116
Wilson B ($Å^2$)	39.05	47.82	27.32
Average B ($Å^2$)^	44.23	55.02	36.53
Protein	44.22	54.95	36.51
Ligands	49.37	64.36	39.68
Water	41.71	51.53	36.70
rmsd bonds (Å)	0.009	0.009	0.009
rmsd angles (°)	1.03	0.98	0.98
Ramachandran plot:			
Favored/outliers (%)	95.63/0.79	94.86/1.58	94.80/2.40

Values in parentheses refer to the highest resolution shell. [+]$R_{merge} = \Sigma|I - <I>| / \Sigma<I>$, where I is the intensity of each individual reflection. *R_{pim} indicates all I[+] & I[-]. [¶]$R_{work} = \Sigma h|F_o - F_c|/ \Sigma_l| F_o|$, where F_o *and* F_c are the observed and calculated structure-factor amplitudes for each reflection h. [#]R_{free} was calculated with 10% of the diffraction data selected randomly and excluded from refinement. ^Calculated using Baverage.

977 **Table S5. Key Resources**

978

REAGENT or RESOURCE	SOURCE or REFERENCE	IDENTIFIER
Bacterial Strains		
E. coli BL21 (DE3)	Invitrogen	Catalogue: C600003
Chemicals		
Benzamidine hydrochloride hydrate	Sigma Aldrich	B6506
Deoxyribonuclease I (DNase I)	Sigma Aldrich	DN25
Ampicillin, Sodium Salt	Astral Scientific	A-1414-25g
Kanamycin Sulfate	Astral Scientific	K-1022-25g
Talon® resin	Clontech	635503
Glutathione Sepharose 4B	GE Healthcare	GEHE17-0756-0
Glutathione (reduced form)	Novachem	Catalogue: 077-02016
Isopropyl β-D-1-thiogalactopyranoside	Bioline	Catalogue: BIO-37036
2-Mercaptoethanol (β-ME)	Sigma Aldrich	Catalogue: M6250-100ML
Triton-X100	Sigma Aldrich	X100-500ML
cOmpleteTM EDTA-free protease inhibitor tablet	Sigma Aldrich	Catalogue: 4693159001
EZ-Link Sulfo-NHS-SS Biotin	Thermo Fisher Scientific	Catalogue: 21217
Synthesised peptides		
FAM21-R5$_{536-552}$ GLFSDEEDSEDLFSSQS	Genscript	N/A
FAM21-R8$_{662-678}$ TSLFEEDEEDDLFAIAK	Genscript	N/A
FAM21-R15$_{1124-1140}$ RGEADLFDSGDIFSTGT	Genscript	N/A
FAM21-R17$_{1197-1213}$ NPFPLLEDEDDLFTDQK	Genscript	N/A
FAM21-R19$_{1261-1274}$ NLFDDNIDIFADLT	Genscript	N/A
FAM21-R20$_{1289-1302}$ SIFDDDMDDIFSSG	Genscript	N/A
FAM21-R20$_{1289-1302\ (IF/SS)}$ S<u>SS</u>DDDMDD<u>SS</u>SSG	Genscript	N/A
FAM21-R21$_{1328-1341}$ SNIFDDPLNAFGGQ	Genscript	N/A
Recombinant DNA		
Plasmid: pET-28a human SNX27 $_{FL}$	Gene Universal	N/A
Plasmid: pET-28a human SNX27$_{FERM}$	Gene Universal	N/A
Plasmid: pGEX4T-2 human FAM21$_{R19-21}$	Gene Universal	
Plasmid: pET-28a human SNX27$_{FL}$ (R437D)	Gene Universal	N/A
Plasmid: pET-28a human SNX27$_{FL}$ (K495D)	Gene Universal	N/A
Plasmid: pET-28a human SNX27$_{FL}$ (K496D)	Gene Universal	N/A
Plasmid: pET-28a human SNX27$_{FL}$ (R498D)	Gene Universal	N/A
Plasmid: pET-28a human SNX27$_{FL}$ (K501D)	Gene Universal	N/A
Plasmid: pEGFP-c1-SNX27 WT and mutants	Simonetti et al 2022	N/A
Plasmid: pEGFP-n1-VPS35 WT and mutants	This study	N/A
Plasmid: pEGFP-c1-Fam21 Tail WT, deletions and mutants	This study	N/A
Plasmid: pXLG3-VPS35-GFP WT and K555N, K556L, K559Q	This study	N/A
Software and Algorithms		
Pymol (version 2.5.4)	Schrodinger, USA.	https://pymol.org/2/
Chimera (version 1.4.0)	Resource for Biocomputing, Visualization, and Informatics,	https://www.cgl.ucsf.edu/chimera/

	University of California, USA	
Prism 7	GraphPad	https://www.graphpad.com/features
Other		
HiLoad® 16/600 Superdex 200 PG	GE Healthcare	Catalogue: 28-9893-35
Mono Q® 10/100 GL	GE Healthcare	Catalogue: 17-5167-01
Amicon™ ultrafiltration devices	Merck	Catalogue: 900000042327 (10K) Catalogue: 900000008078 (30K)
SDS-PAGE BOLT gels	Thermo Fisher Scientific	Catalogue: NW04122BOX (12-well)
NuPAGE 4-12% gels	Thermo Fisher Scientific	Catalogue: NP0336
NuPAGE MOPS SDS running buffer	Thermo Fisher Scientific	Catalogue: NP000102
ChromoTek GFP-Trap Agarose beads	ProteinTech	Catalogue: gta
Streptavidin Sepharose beads	Cytiva	Catalogue: 90100484

979

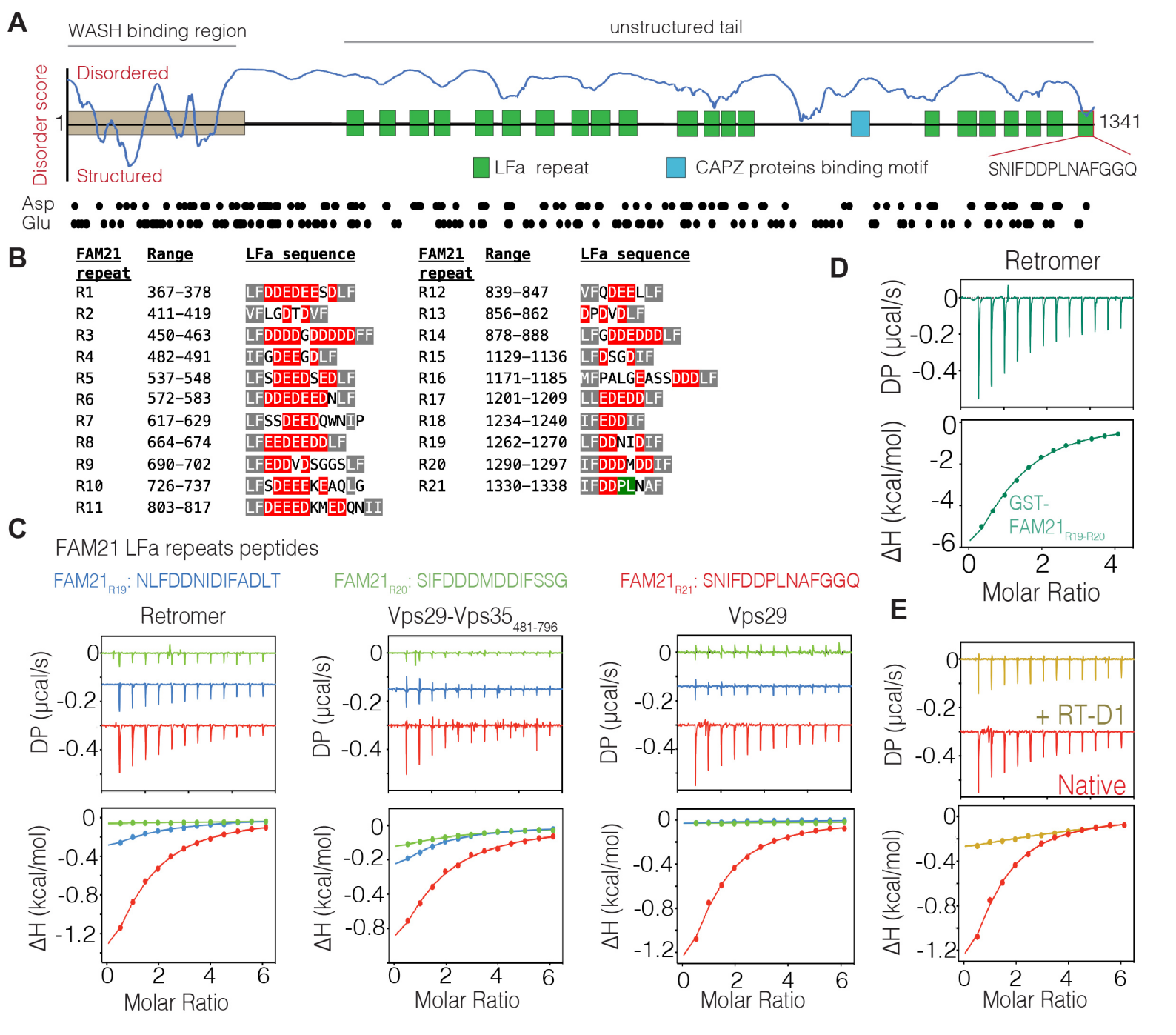

Figure 1. Retromer VPS29 is responsible for binding to repeat 21 of FAM21.
(A) Schematic diagram showing features of human FAM21, and highlighting the 21 LFa repeats in the unstructured tail. (B) Sequences of the 21 LFa repeats within the FAM21 tail. Conserved [I/L]F residues are shown in grey and acidic residues are in red. The PL residues of repeat 21 are highlighted in green. (C) ITC thermograms showing the titration of Retromer, the VPS29–VPS35481-796 subcomplex, and VPS29 alone with FAM21R19 (blue); FAM21R20 (green); and FAM21R21 (red) peptides. (D) Retromer shows binding to GST-FAM21R19-R20. (E) VPS29 and FAM21R21 peptide interaction can be blocked by the addition of the PL-sequence containing cyclic peptide RT-D1. All ITC graphs show the integrated (bottom) and normalized raw data (top) fit with a single-site binding model.

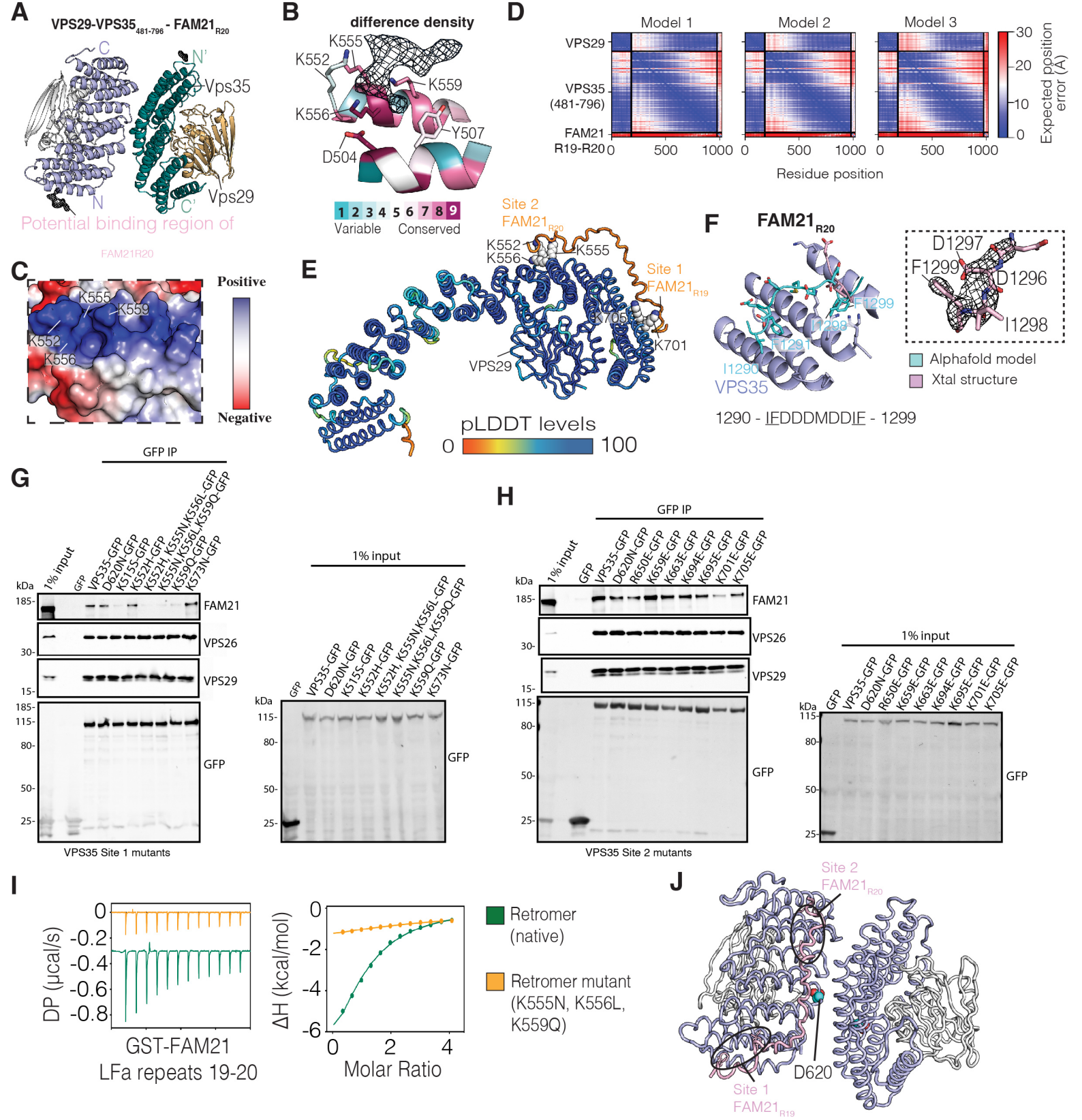

Figure 2. Structural basis for the interaction of LFa repeats with Retromer subunit VPS35.
(A) Overall crystal structure of VPS29–VPS35481-796 in complex with FAM21R20 peptides showing both complexes from the asymmetric unit. (B) VPS35 is highly conserved in the FAM21R20 binding region. The density corresponding to the FAM21R20 peptide is shown in mesh using 2Fo–Fc map contoured at 1σ. Sequence conservation of VPS35 was mapped with CONSURF (Ashkenazy et al., 2016). (C) The electrostatic surface map showing FAM21R20 binding location on VPS35. (D) Predicted alignment Error (PAE) plots of VPS29–VPS35481-796–FAM21R19-R20 complexes generated by Alphafold2. (E) The predicted structure highlighting the per-residue confidence score (pLDDT) between 0 to 100. Regions showing low pLDDT score (green and orange) are likely to be unstructured. (F) Alignment of the Alphafold2 model of FAM21R20 (cyan) and the crystal structure (VPS35 in light purple, FAM21R20 as light pink) highlighting the key interacting residues between FAM21R20 and VPS35. The insert shows the refined electron density of the FAM21R20 peptide observed in the crystal structure. (G) Co-immunoprecipitation (co-IP) of C-terminal GFP-tagged VPS35mutants in the Site 2 binding pocket in HEK293T cells. (H) Co-IP of C-terminal GFP-tagged VPS35 and mutants in the Site 1 binding pocket. Quantitation of these Western blots is shown in Figure S2. (I) ITC analysis showing the binding of GST-FAM21R19-R20 with either native Retromer or VPS35 (K555N/K556L/K559Q) Site 2 mutant. All ITC graphs show the integrated (bottom) and normalized raw data (top) fit with a single-site binding model. (J) The locations of the Site 1 and Site 2 FAM21 repeat binding sites are shown in the context of the VPS35-mediated Retromer dimer assembly derived from cryoelectron tomography (Leneva et al., 2021). The location of the D620N mutation linked to Parkinson's Disease is also indicated in cyan spheres.

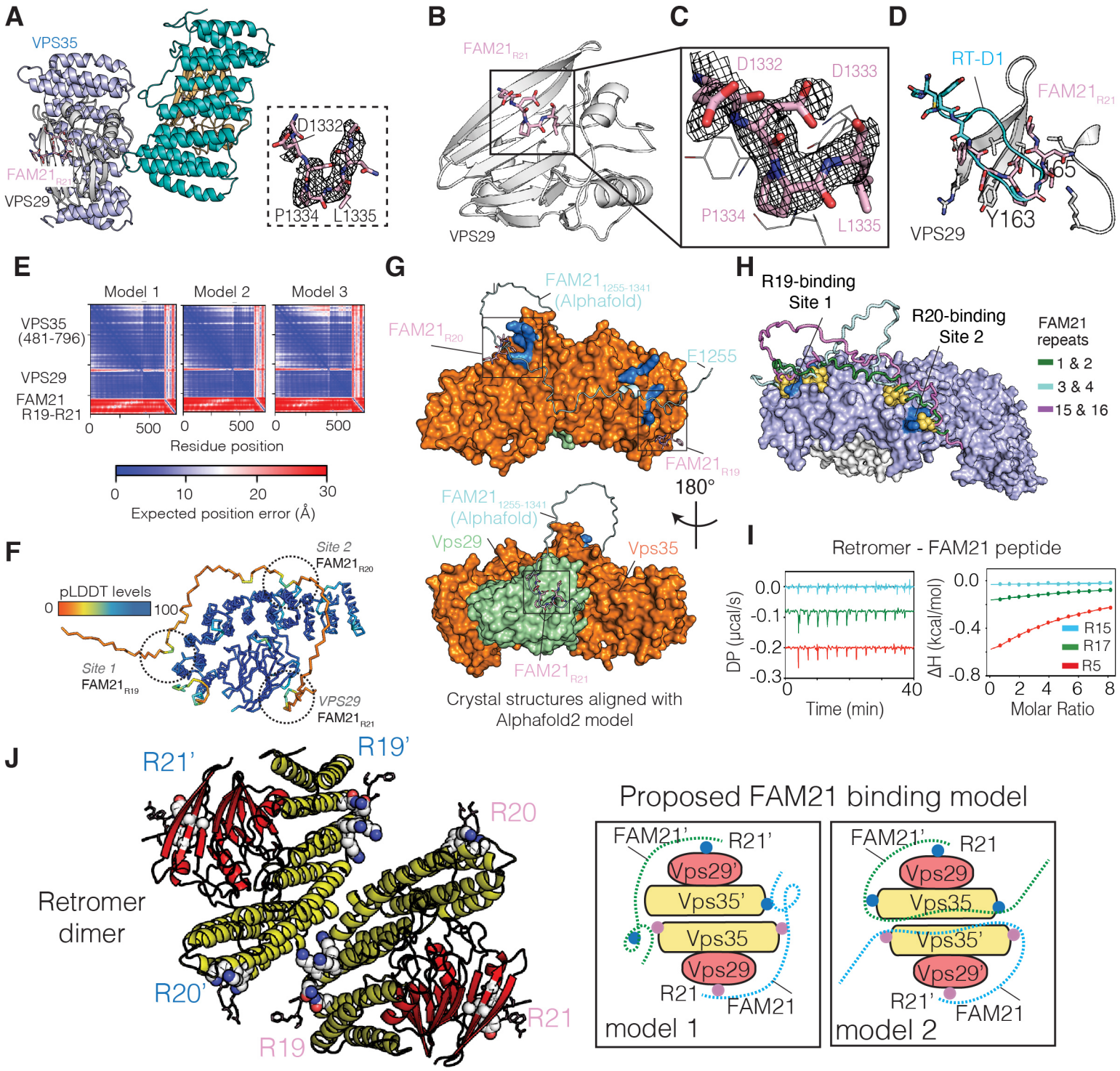

Figure 3. Structural basis for repeat 21 binding to VPS29 and model for Retromer engagement by multiple FAM21 repeats.
(A) Crystal structure of VPS29–VPS35481-796 bound to the FAM21R21 peptide. (B) Crystal structure of VPS29 in complex with FAM21R21 peptide. (C) Enlarged view highlighting the refined density of FAM21R21 peptide peptide (2Fo–Fc map contoured at 1σ). (D) Structural alignment of the VPS29–FAM21R21 peptide complex with the VPS29–RT-D1 cyclic peptide complex (PDB ID 6XS5)(Chen et al., 2021) highlighting the PL motif binding region. (E) Predicted alignment Error (PAE) plots showing the predicted structure of VPS29–VPS35481-796–FAM21R19-R21 complex generated by Alphafold2. (F) The predicted structure highlighting the per-residue confidence score (pLDDT) between 0 to 100. Regions showing low pLDDT score (represents as green and orange) are likely to be unstructured. (G) Superimposition of all the two crystal structures with the Alphafold2 model. (H) Alphafold2 predictions of the complex of VPS29–VPS35 with either FAM21R1-R2, FAM21R3-R4 or FAM21R15-R16 showing pairs of repeats predicted to bind to the same positively charged grooves as repeats FAM2119-20. (I) ITC thermogram showing the binding between Retromer with FAM21R5 (red line), FAM21R15 (blue line) and FAM21R17 (green) peptides. All ITC graphs show the integrated (right) and normalized raw data (left) fit with a single-site binding model. (J) The locations of the FAM21 repeat 19 and 20 binding sites as well as the VPS29-binding repeat 21 are shown in the context of the VPS35-mediated Retromer dimer assembly derived from cryoelectron tomography (Leneva et al., 2021) (PDB ID: 7BLN). The right panel shows two proposed binding models for how FAM21 can bind to a Retromer dimer in cis or trans.

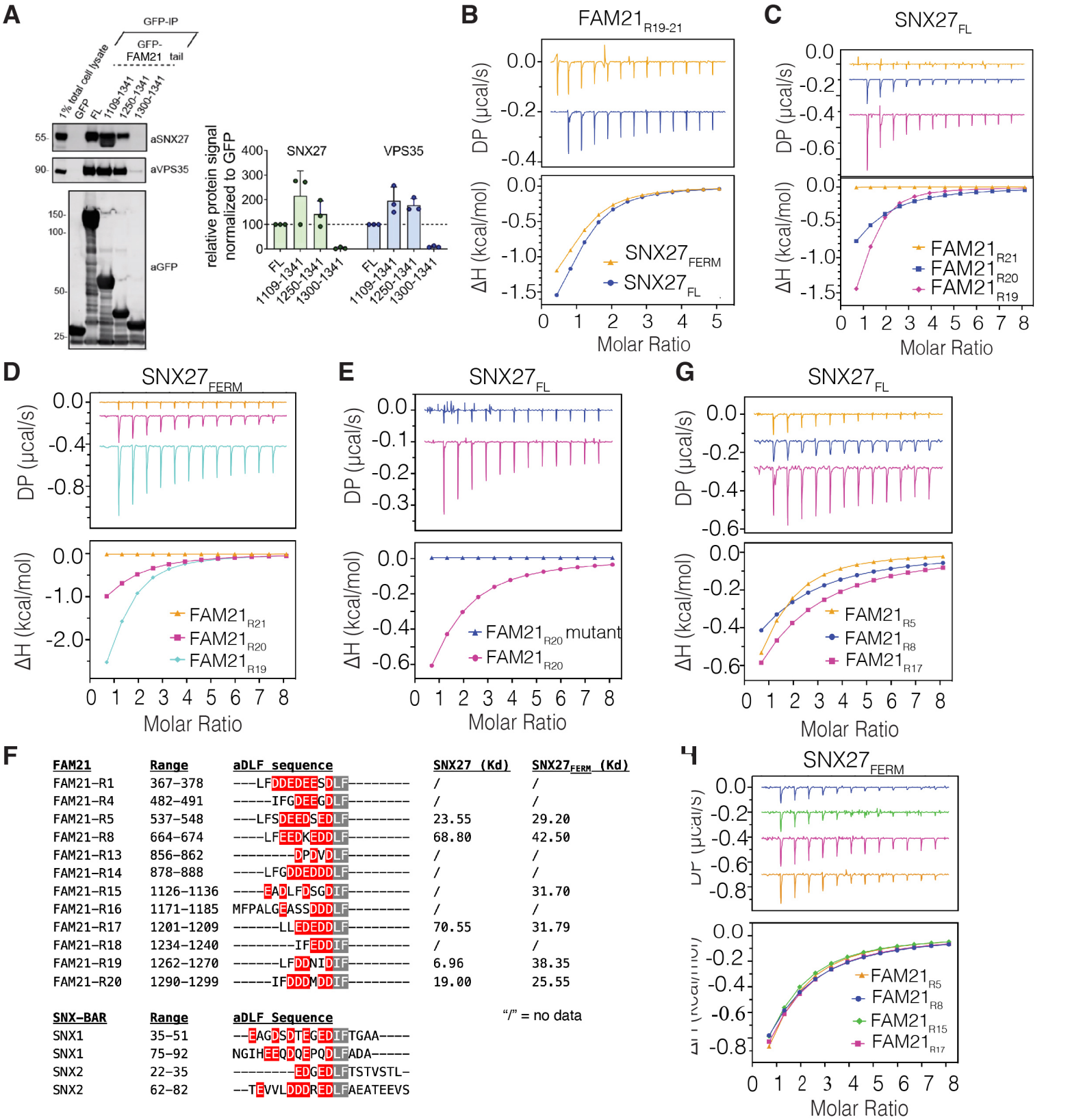

Figure 4. FAM21 aDLF repeats also binds to the SNX27 FERM domain.
(A) Co-IP of GFP-tagged FAM21 tail in HEK293T cells. Samples were analysed by quantitative fluorescence-based western blotting. The band intensities of SNX27 and VPS35 were measured from n=3 independent experiments using Odyssey software. The SNX27 and VPS35 band intensities, normalized to GFP expression, are presented as the average fraction of the full length FAM21 tail. (B) ITC analysis showing the binding between GST-FAM21R19-21 and SNX27 (yellow line) and SNX27 FERM (blue line). (C) Similar binding experiment showing the binding of FAM21 peptides FAM21R19, FAM21R20 and FAM21R21 with either (C) SNX27 FL or (D) SNX27 FERM. (E) ITC thermogram comparing the binding between native FAM21R20 and 1298IF1299 to SS mutant peptides with SNX27 FL. (F) List of FAM21 peptides containing the same aDLF motif to those observed in SNX1 and SNX2. (G) ITC binding curves of the FAM21R5, FAM21R8 and FAM21R17 peptides titrated into either (G) SNX27 FL or (H) SNX27 FERM. All ITC graphs show the integrated (bottom) and normalized raw data (top) fit with a single-site binding model.

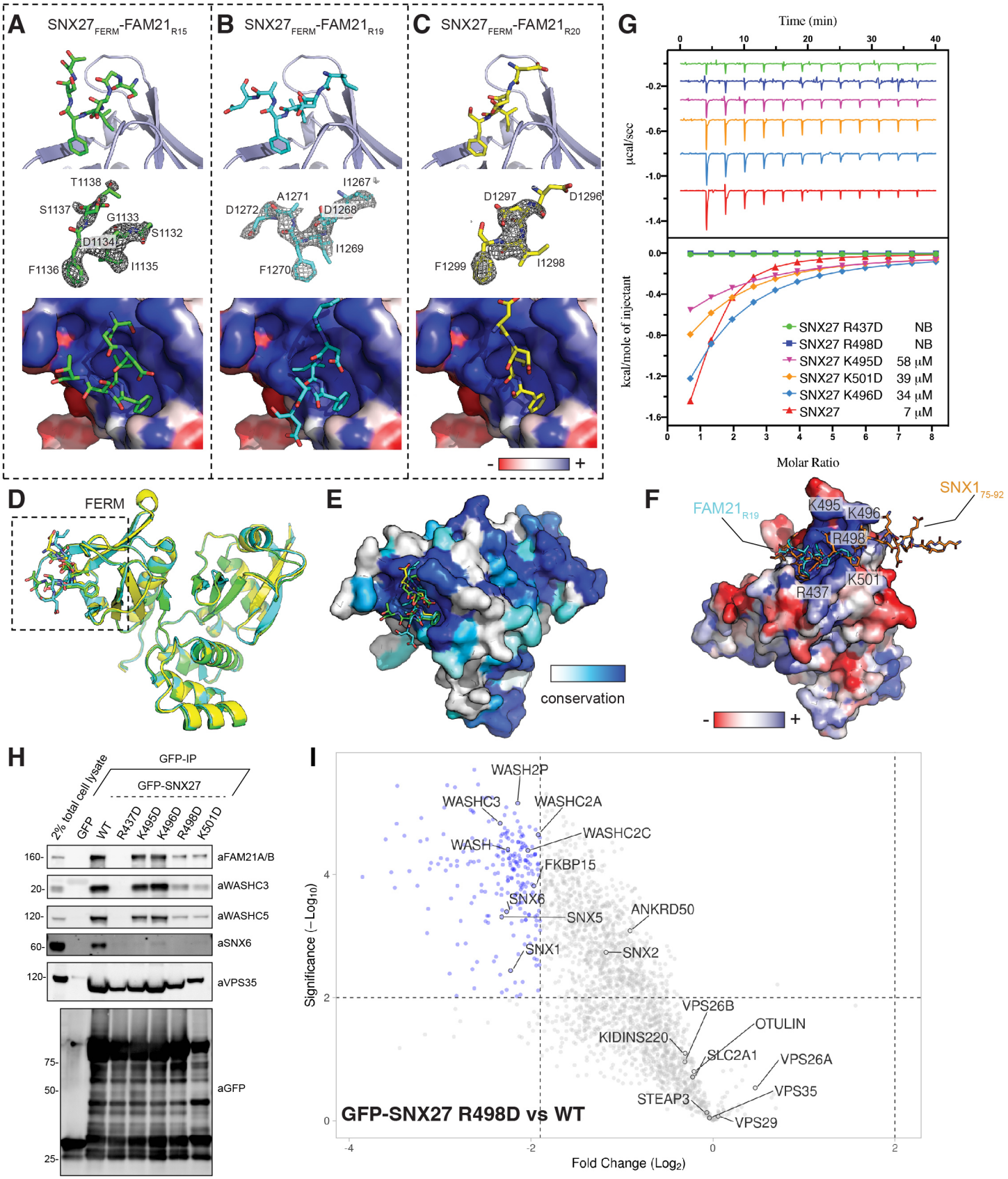

Figure 5. Structural basis for SNX27 interaction with FAM21 aDLF repeats.
(A) Crystal structures of the SNX27 FERM domain bound to aDLF repeats of FAM21. Top views show the key region of SNX27 FERM involved in the binding to the FAM21 aDLF seqeunces (A) FAM21R15, (B) FAM21R19 and (C) FAM21R20. Middle panels show the electron density corresponding to a simulated-annealing composite omit 2Fo–Fc map contoured at 1σ. Bottom panels show electrostatic surface potential of SNX27 highlighting the positively charged pocket of SNX27 FERM. (D) Structural alignment showing the high degree of similarity between all three complex structures. (E) Sequence conservation map highlighting the conserved pocket of SNX27 FERM domain for binding to FAM21 aDLF motifs. (F) Structural alignment of SNX27 bound to FAM21R19 with the SNX27–SNX175-92 complex (PDB ID 7CT1; (Yong et al., 2021)) showing they bind the same pocket. (G) ITC analysis showing the binding of the FAM21R19 peptide with the native or mutant forms of SNX27. The ITC graphs represent the integrated and normalized data fit with 1:1 ratio binding. (H) Co-IP of GFP-SNX27 mutants and binding of WASH, Retromer and ESCPE-1 (represented by SNX6) proteins assessed by Western blot. (I) Proteomic studies comparing the native SNX27 and mutated SNX27 R498D binding capabilities with SNX27 interactors assessed by Co-IP (n = 6; derived from 2 biological repeats each with 3 technical repeats). Mutation of the aDLF binding pocket causes disrupted interactions with most WASH and ESCPE-1 subunits. The full list of detected proteins is provided in Dataset S1.

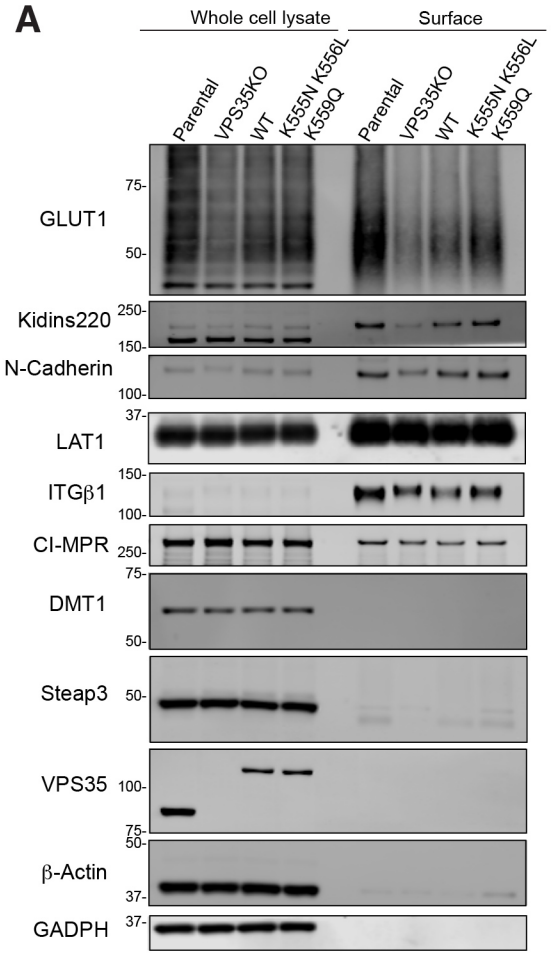

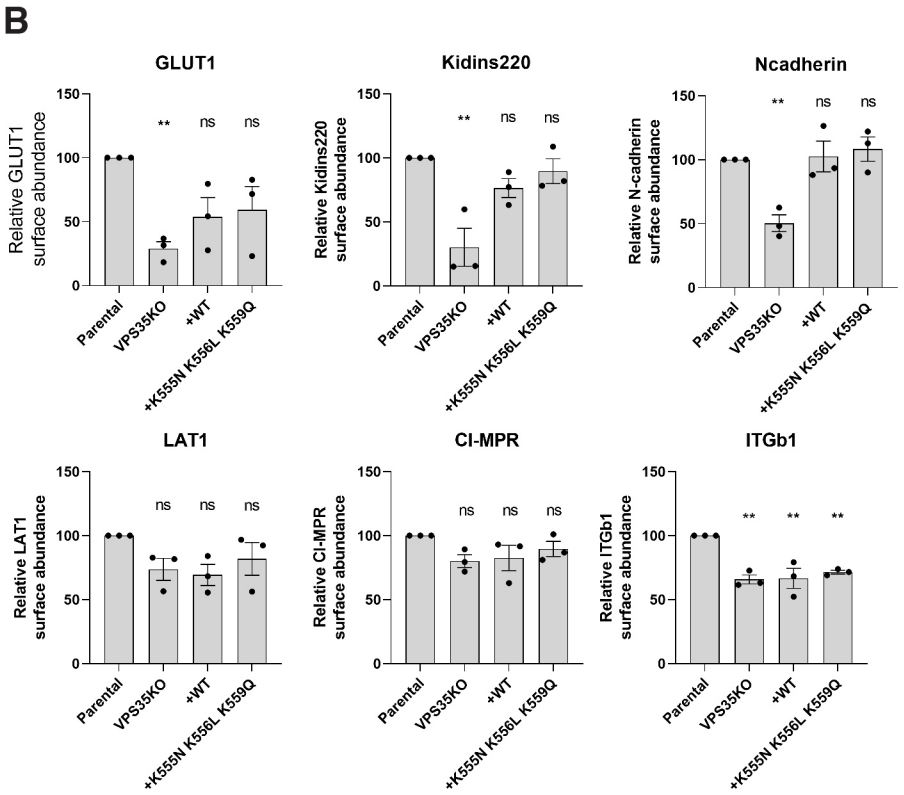

Figure 6. VPS35 interaction with FAM21 alone is not strictly required for SNX27–Retromer recycling.
(A) VPS35 KO HeLa cells showed reduced cell surface levels of SNX27–Retromer dependent cargos including GLUT1 and KIDINS220. VPS35 KO clonal line was stably transduced with lentiviral particles containing VPS35-GFP WT or VPS35(K555N, K556L and K559Q), the mutation of the primary FAM21 binding Site 2. Re-expression and rescue with both constructs is able to rescue the cell surface levels of these cargos. This indicates that full binding of FAM21 to VPS35 is not strictly required for SNX27–Retromer mediated endosomal recycling. (B) Quantitation of Western blots is shown. Similar results were obtained in H4 cell lines as shown in Figure S5C.

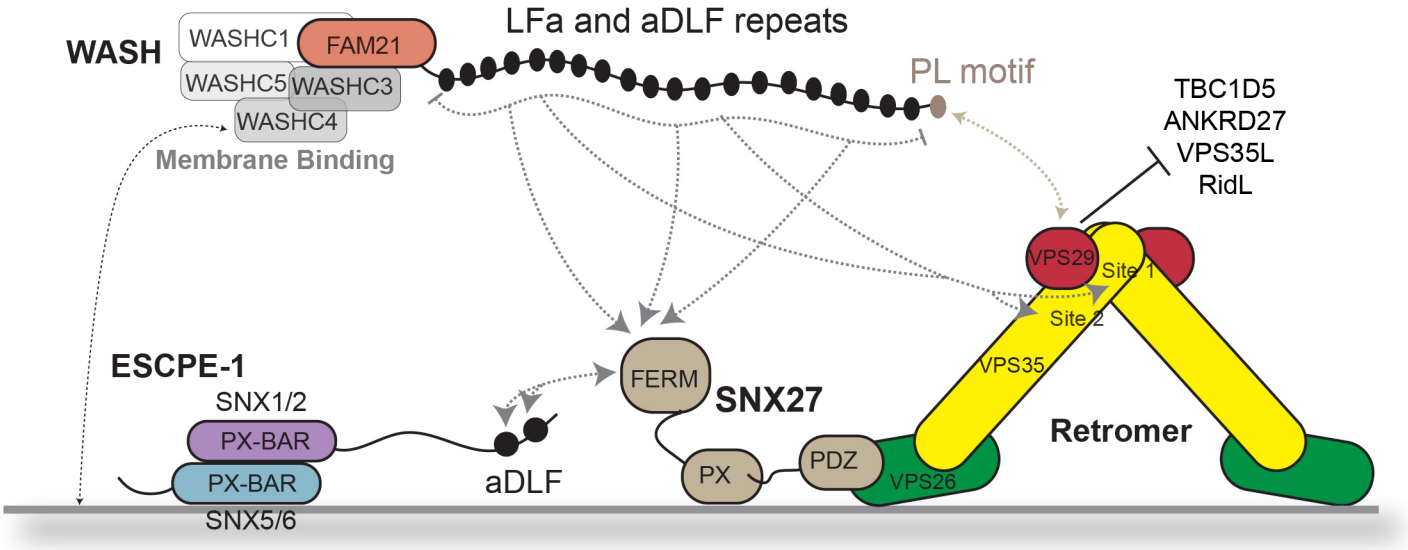

Figure 7. Summary and proposed model for the cooperative recruitment of FAM21 by Retromer, SNX27 and other endosomal proteins. The WASH subunit FAM21 has 21 LFa repeated elements in its extended tail that are rich in acidic, isoleucine and phenylalanine residues. LFa sequences possess two [L/I]F motifs interspersed by an acidic stretch ([L/I]F[D/E]3-9[L/I]F). These bind two conserved sites towards the C-terminus of the VPS35 subunit of Retromer. The last repeated element of FAM21 has a specific PL dipeptide sequence that promotes interaction with Retromer subunit VPS29. This would be mutually exclusive of binding to other VPS29 interactors such as TBC1D5, ANKRD27, VPS35L and bacterial effector RidL. aDLF sequences are a subset of the LFa repeats with an acidic stretch prior to a D[L/I]F motif that associate with a conserved pocket in the SNX27 FERM domain, and are also found in the SNX1 and SNX2 proteins of the ESCPE-1 complex.

```
hFam21     1  SNLFDDNIDIFADLT..VKPKEK.SKKKV.EAKSIFD..DDMDDIFSSG.....IQAK
mFam21     1  PNLFDDNIDIFADLT..VKPKEK.SKKKV.AAKSMFD..DDTDDIFSSG.....LQAK
rFam21     1  PNLFDDNIDIFADLT..VKPKEK.PKKKV.TAKSMFD..DDTDDIFSSG.....LQAK
bFam21     1  SNLFDDNIDIFADLT..VKPKEK.SKKKV.EAKSIFD..DDTDDIFSSG.....IQTK
dFam21     1  TSLFSSD.DEEAEVP..VKSAPA.KKLPVKPSKSLFSDDDDDDDLFGGSSTSKAAAK
zfFam21    1  ASLFDDDVDIFADLTGTSKPKEKKAKKKV.ETKSIFD..DDMDDIFSTG.....TTKP
```

Repeat 19 Repeat 20

```
hFam21    48  TTKPKSRSAQA..APEPRF.EHK....VSNIFDDPLNAFGG.Q
mFam21    48  ASKPKSQSAEA..ASEQRS.EHK....VASIFDDPLNAFGS.Q
rFam21    48  ASKPKSQSAEA..VSELRS.ENK....VSNIFDDPLNAFGS.Q
bFam21    48  TTKSKSRSSQK..VTESRS.GQK....VSNIFDDPLNAFGG.Q
dFam21    55  KTKPAARTASK..PPASKT.TTPTATIPSNSGDNPLADLLDFK
zfFam21   51  TVKPSSKSKKSQPIQEPASTAET....AHNIFDDPLNAFGG.N
```

Repeat 21

Figure S1. Sequence alignment of FAM21/WASHC2 repeats 19, 20 and 21.
Repeats 19-21 of FAM21 are aligned from various species. Conserved [I/L]F dipeptide motifs are indicated by yellow arrows while the specific PL motif in repeat 21 is indivated by green ovals. h, homo sapiens; m, Mus musculus; r, Rattus norvegicus; b, Bos taurus; d, Drosophila melanogaster; zf, Danio rerio.

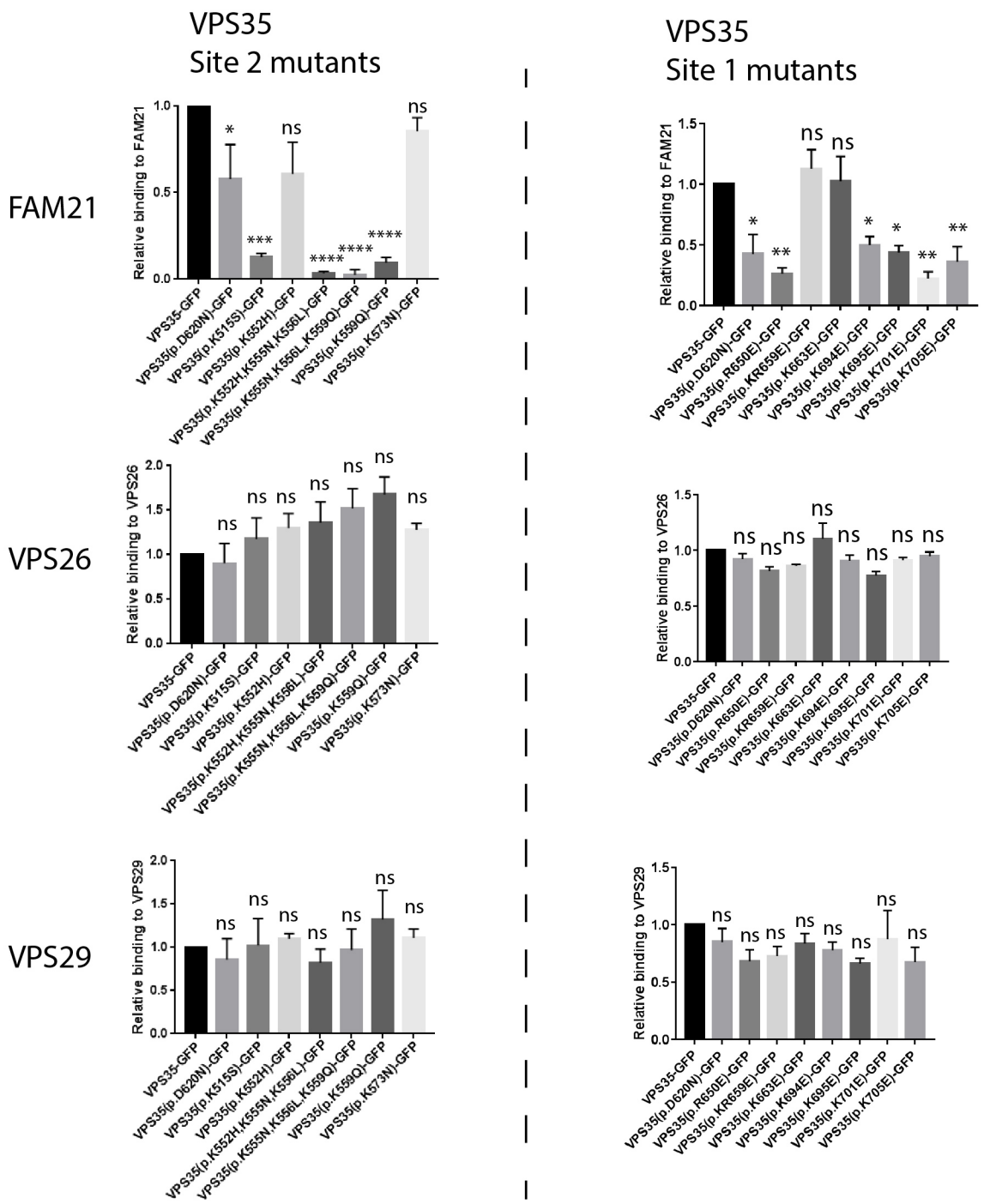

Figure S2. Quantitation of the Western blots shown in Figure 2G and 2H.
Band intensities from Figure 2G and 2H were quantified using Odyssey software and normalized to GFP expression. 1-way ANOVA with Dunnett's multiple comparisons test. Error bars represent the standard error. *P < 0.05, **P < 0.01, ***P < 0.001, ****P < 0.0001.

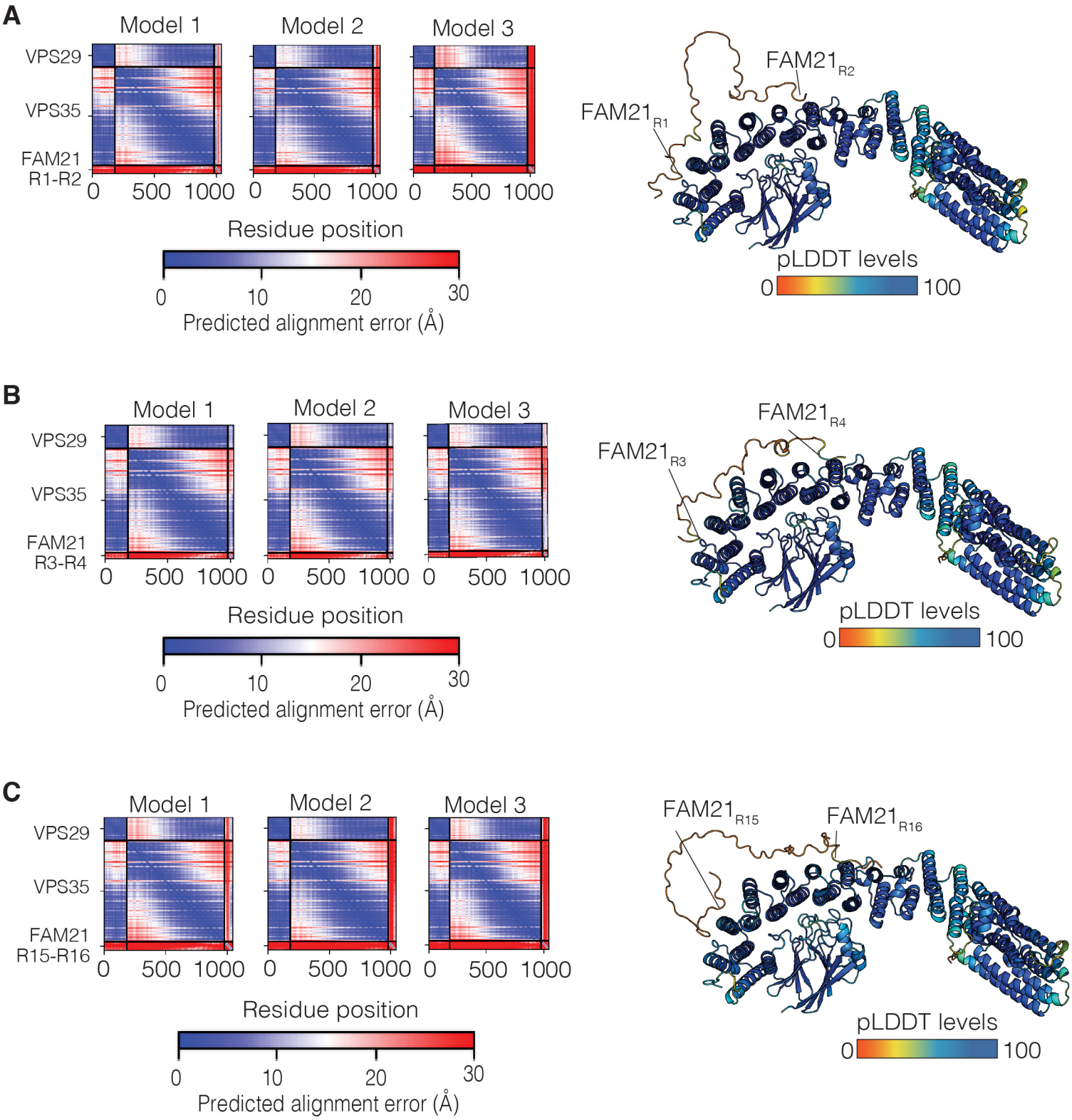

Figure S3. Alphafold models of VPS35–VPS29 in complex with different FAM21 LFa repeats.
(A) Predicted alignment Error (PAE) plots for the AlphaFold2-predicted structures of the human (A) VPS35–VPS29–FAM21R1-R2 complex, (B) VPS35–VPS29–FAM21R3-R4 complex, (C) VPS35–VPS29–FAM21R15-R16 complex. On the right the predicted structures are shown coloured according to the per-residue confidence score (pLDDT) between 0 to 100. Regions showing a low pLDDT score (green and orange) are likely to be unstructured.

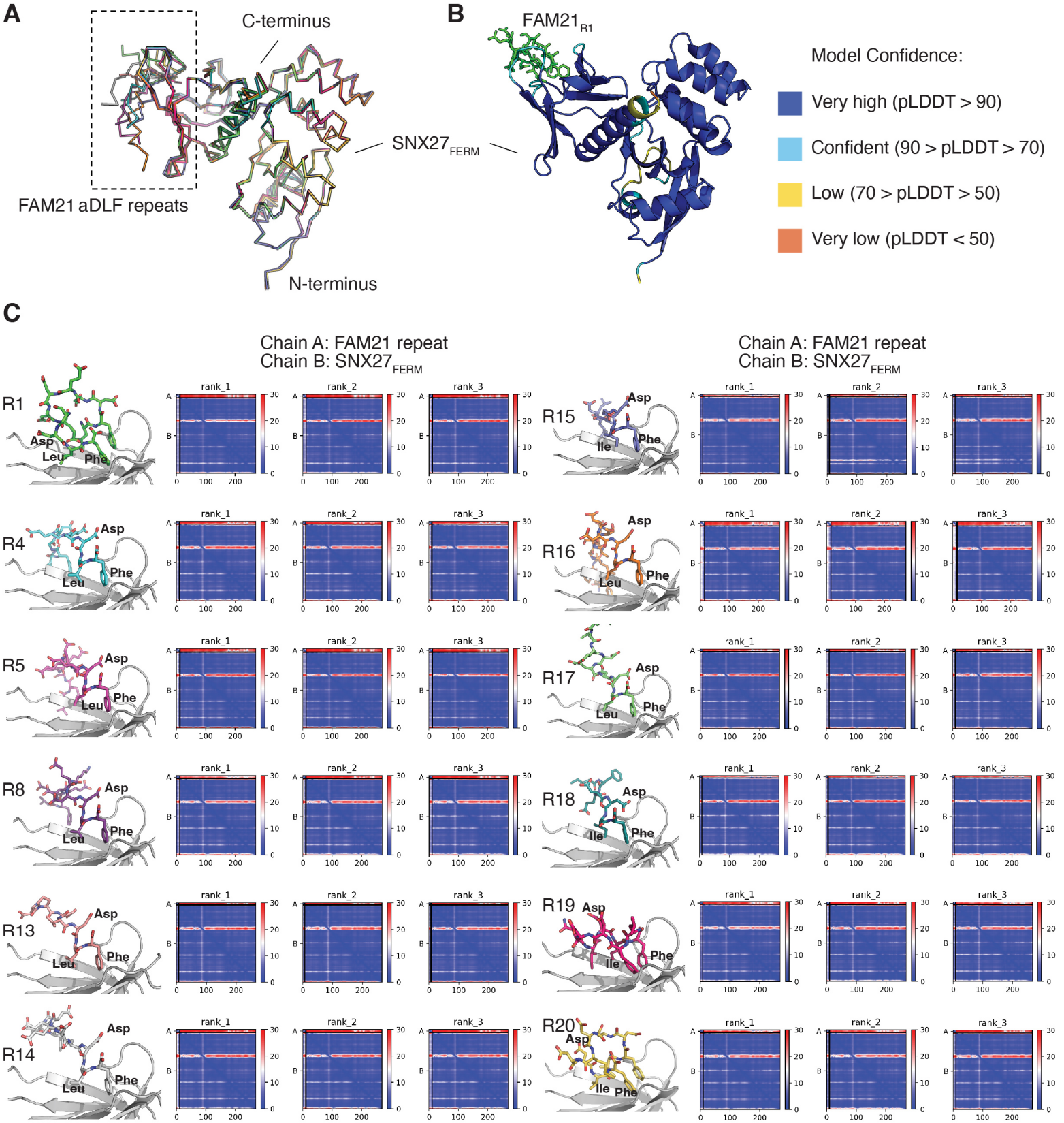

Figure S4. Alphafold models of SNX27 FERM domain in complex with various FAM21 aDLF sequences.
(A) Overlay of all AlphaFold2 predicted structures shown as Cα backbone ribbon. The sequences of the aDLF repeats are shown in Figure 4F. (B) The predicted complex of SNX27FERM bound to FAM21 aDLF sequence from repeat 1. SNX27 is shown in cartoon representation coloured according to pLDDT score. The FAM21R1 peptide is shown in green sticks. (C) Predicted alignment Error (PAE) plots showing the predicted structure of human SNX27FERM–FAM21 aDLF complexes. The top ranked prediction is shown in close up in the left hand panels.

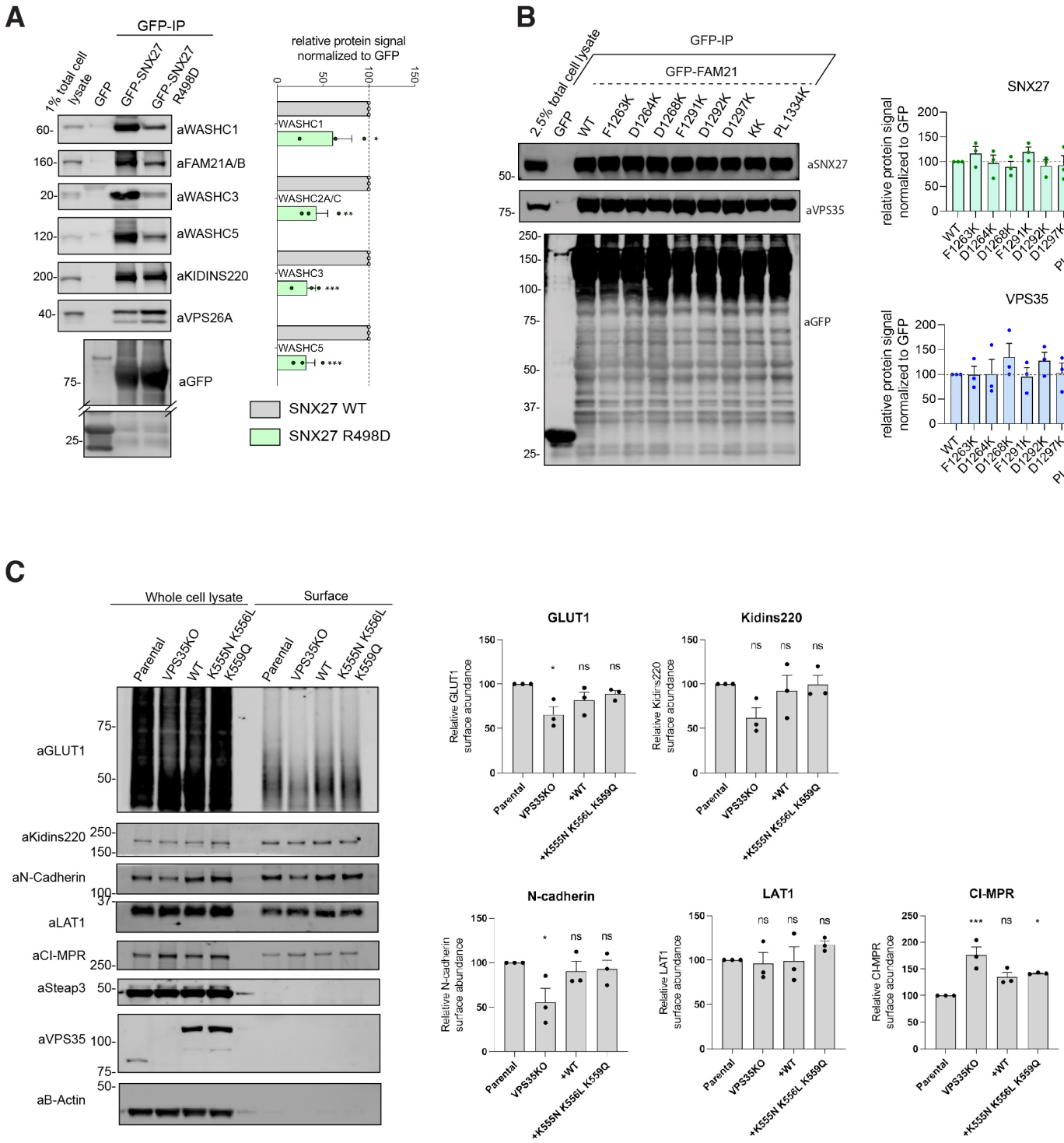

Figure S5. Interactions of SNX27 and FAM21 mutants and VPS35 rescue experiments in H4 cells.
(A) Co-IP of GFP-SNX27 wild-type and R498D mutant and binding of WASH, Retromer (indicated by subunit VPS26A) and model cargo KIDINS220 assessed by Western blot. (B) Co-IP of GFP-FAM21 and mutants shows that specific mutations in repeats 19-21 do not prevent binding to Retromer or SNX27 in cells. KK is the combination of D1268K and D1297K mutants. (C) VPS35 KO H4 cells showed reduced cell surface levels of SNX27–Retromer dependent cargos including CTR1, GLUT1 and KIDINS220. Re-expression and rescue with both GFP-VPS35 wild-type protein and GFP-VPS35(K555N, K556L and K559Q) with mutation of the FAM21 binding Site 1 is able to rescue the cell surface levels of these cargos. This indicates that Site 2 in VPS35 is not strictly required for SNX27–Retromer mediated endosomal recycling. Band intensities for all blots were quantified using Odyssey software and normalized to GFP expression. 1-way ANOVA with Dunnett's multiple comparisons test. Error bars represent the mean, s.d. *P < 0.05, **P < 0.01, ***P < 0.001, ****P < 0.0001.